Article

Tempo-Spatial Tungsten Metallogeny in the Xing'an–Mongolia Orogenic Belt: Insights from the Early Cretaceous Shamai Tungsten Deposit Case Study in Northeastern China

Zhenjiang Liu [1],*, Jianping Wang [1],*, Shaobo Cheng [2],[3] and Jiajun Liu [1]

1. School of Earth Sciences and Resources, China University of Geosciences, Beijing 100083, China; liujiajun@cugb.edu.cn
2. International Mining Research Center, China Geological Survey, Beijing 100037, China; chengshaobo0631@sina.com
3. China Mining News, Beijing 100037, China
* Correspondence: lzj@cugb.edu.cn (Z.L.); jpwang@cugb.edu.cn (J.W.)

Abstract: The Xing'an–Mongolia Orogenic Belt (XMOB) is located in the eastern part of the Central Asian Orogenic Belt (CAOB). The region's notable tectonic complexity and extensive tungsten mineralization offer a unique opportunity to explore metallogeny mechanisms in orogenic areas. This study focuses on the Shamai tungsten deposit as a case study, presenting results from LA–ICP–MS U–Pb dating of fine-grained, medium-grained, and porphyritic biotite monzogranite samples from the deposit, along with in situ zircon Hf isotopic and plagioclase Pb isotopic analyses. The fine-grained, medium-grained, and porphyritic biotite monzogranite were emplaced at 142.5, 141.9, and 140.2 Ma, respectively. These samples contain zircons with εHf(t) values ranging from 3.2 to 7.9 and 4.2 to 7.6, respectively, yielding T_{DM2} model ages from 996 to 692 Ma and 923 to 708 Ma. These findings suggest that the magmas in the Shamai deposit were produced by partial melting of juvenile crustal material mixed with mantle-derived components. The tungsten mineralization periods in the Eastern XMOB region can be divided into three stages: Early Paleozoic (ca. 520–475 Ma), Triassic (ca. 250–200 Ma), and Jurassic to Early Cretaceous (ca. 190–130 Ma). The highest concentration of tungsten mineralization in the XMOB occurs within the Xing'an Block during the Jurassic to Early Cretaceous period. Yanshanian magmatism and the most significant tungsten metallogenic events are likely influenced by an extensional setting and oceanic slab rollback, shaped by the tectonic evolution of the Mongol-Okhotsk Ocean and the Paleo-Pacific Ocean.

Keywords: Shamai tungsten deposit; mineralization mechanism; Nd–Hf–Pb isotopes; metallogenic geodynamics; Xing'an–Mongolia Orogenic Belt; Central Asian Orogenic Belt

1. Introduction

The Central Asian Orogenic Belt (CAOB) is the largest accretionary orogen in the world (Figure 1a). Its formation, evolution, tectonic superimposition, and evolutionary history have always been hot topics in geosciences [1–3]. The Xing'an–Mongolia Orogenic Belt (XMOB) is located in the eastern part of the CAOB and lies between the North China Craton (NCC) and the Siberian Craton. It preserves a complex record of tectonic and magmatic events (Figure 1a,b) [4–6]. The XMOB underwent a significant transformation in the tectonic domain of the northwestern Mongol-Okhotsk Ocean and the eastern Paleo-Pacific plate during the Mesozoic after initially forming in the Paleozoic [6,7]. As a crucial

metallogenic belt in northern China, the XMOB hosts numerous ore deposits of Pb–Zn–Ag, Cu, W, Sn, Mo, Au, Fe, and others [8].

China currently dominates the world's production of tungsten due to its possession of the largest tungsten reserves in the world [9]. More than 90% of global tungsten resources are concentrated in Nanling and adjacent areas in southern China [10]. Additionally, the XMOB has dozens of tungsten ore deposits of varying sizes (Figure 1b), including the Honghuaerji porphyry-type deposit [11,12], the Cuihongshan skarn-type deposit [13,14], and the Shamai deposit hosted by greisen-related quartz vein [15–18], among others. In comparison to the Nanling region, which is characterized by a discernible temporal concentration of tungsten mineralization, substantial mineralization intensity, and a profound association with the regional granites [19], the XMOB area presents a distinctly different geological scenario. Controlled by the intricate interplay of multi-terrane integration and a complex tectonic evolution [6,7], the XMOB region shows a lower degree and intensity of tungsten mineralization. On the other hand, it makes up for it by having a more comprehensive range of genetic types of tungsten mineralization. Moreover, the XMOB region exhibits an extensive metallogenic timespan covering the Paleozoic and Mesozoic eras [8]. This highlights a prolonged and diverse geological history in contrast to the more temporally concentrated mineralization events observed in the Nanling area.

The remarkable tectonic complexity and long-span mineralization of tungsten in the XMOB offer an unparalleled opportunity to explore the mechanisms of metallogeny in orogenic regions. Our case study focused on the Shamai tungsten deposit. We obtained new U–Pb ages for fine-grained biotite monzogranite, medium-grained biotite monzogranite, and porphyritic biotite monzogranite units associated with the Shamai tungsten deposit using zircon laser ablation–inductively coupled plasma mass spectrometry (LA–ICP–MS). Additionally, we collected new data on in situ zircon Hf isotopic and in situ plagioclase Pb isotopic samples. These data help us determine the emplacement timing of the intrusions and offer insights into the origin of the various stages of mineralization-related magmatism in this area. Then, we compiled seventeen additional tungsten deposits in the XMOB, as shown in Table 1 and Figure 1c. Based on the published literature (Table 1), geochemical data from ore-forming granites in the XMOB's tungsten deposits were collected, as most tungsten resources originate from granite-related deposits [20]. This enabled a detailed discussion of the main genetic types of tungsten mineralization events and analyzed their spatial and temporal patterns. The findings helped identify the principal stages of tungsten mineralization in the XMOB, offering a thorough assessment of the distribution, intensity, magnitude, and genetic diversity of deposits for each distinct metallogenic phase. Additionally, the study examined the role of different granite types in tungsten mineralization and compared the tectonic settings underlying mineralization across various geological periods. These insights were synthesized to construct a coherent framework summarizing the governing principles of tungsten mineralization within accretionary orogenic belts.
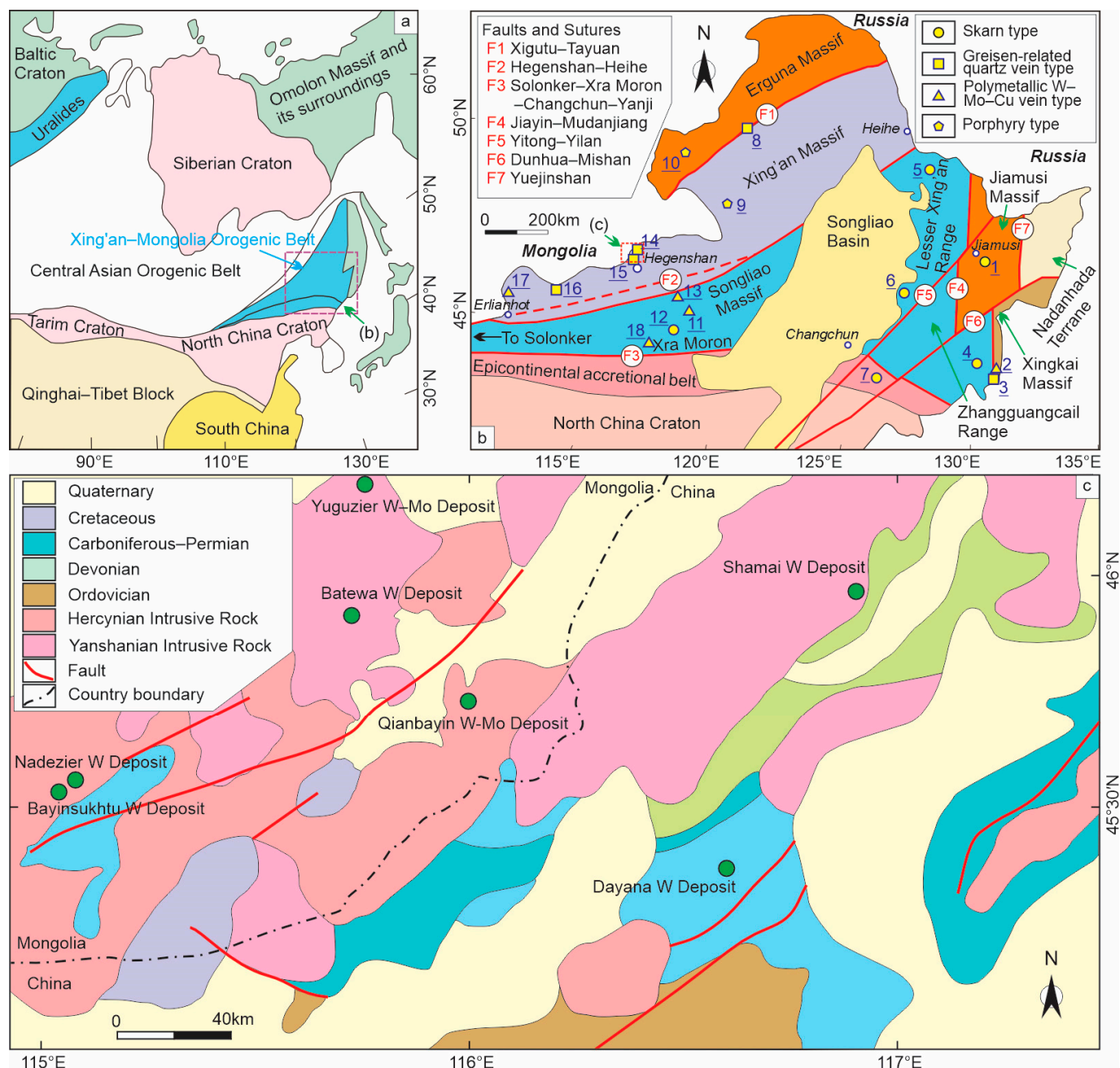
Figure 1. (**a**) Schematic geological map of the Central Asian Orogenic Belt (modified from [21]). (**b**) Geological map of the Great Xing'an Range and adjacent areas (Xing'an–Mongolia Orogenic Belt) in NE China (modified from [21]), including the locations of major tungsten deposits. (**c**) Regional geological map of the Shamai tungsten deposit (modified from [22]). Tungsten deposits shown in (**b**) are as follows: 1—Yangbishan; 2—Yangjingou; 3—Wudaogou; 4—Baishilazi; 5—Cuihongshan; 6—Gongpengzi; 7—Sanjiazi; 8—Weilianhe; 9—Dongshanwan; 10—Honghuaerji; 11—Daolundaba; 12—Huanggang; 13—Weilasituo; 14—Shamai; 15—Dayana; 16—Baogeda Ula; 17—Wurinitu; 18—Chamuhan.

Table 1. Types, tonnage, grade, and characteristics of tungsten deposits in the XMOB, northeast China.

Deposit (No. in Figure 1)	Location	Commodity	Size	Grade (WO₃, %)	Ore-Forming Intrusions (Ma)	Wall-Rock Alteration	Ore Mineral Assemblage	Gangue Mineral Assemblage	Ore-Forming Ages (Ma)	References
					Skarn type					
Yangbishan (1)	Center of the Jiamusi Massif	Fe–W	Medium	0.38	Gneissic granite (520.6 ± 2.8)	SK, SI, AC, CA, CH, EP, FL	Sch, Pyh, Py, Ccp, Sp, Cst, Apy	Aug, Qtz, Di, Pl, Grt, Tr, Act, Chl, Ep, Kfs, Ves, Tur, Fl	-	[23–25]
Baishilazi (4)	Eastern part of Jiamusi–Xingmeng Terrane	W	Medium	0.99	Quartz diorite (198.27 ± 0.80)	SK, SI, CH, SE, CA	Sch, Ccp, Py, Pyh	Gro, Hd, Di, Ep, Cal, Qtz	-	[23,26]
Cuihongshan (5)	Northern segment of the Lesser Xing' an-Zhangguangcai Range	Fe–W–Mo–Zn–Cu–Ag	Large	0.153	Granodiorite (493 ± 4) Monzogranite (194 ± 1) Alkali-feldspar granite (204 ± 1)	KF, AL, SI, FL, CA	Sch, Mol, Gn, Sp, Mag	Grt, Di, Tr, Act, Ep, Chl, Fl, Qtz, Pl, Cal, Phl, Ves, Ilv, Srp, Dol	205 ± 2 204 ± 4 195.4 ± 1.9 191.2 ± 7.5	[23,27,28]
Sanjiazi (7)	Southwestern segment of the Heilongjiang–Jilin Orogenic Belt	W	Small	-	Porphyritic granite (172.4 ± 1.8 Ma)	AL, KF, SK, SI, CH, CA	Py, Sch, Wfm, Bin, Mol, Ccp, Pyh	Fsp, Qtz, Bt, Grt, Act, Ep, Chl, Cal	-	[29,30]
Gongpengzi (6)	The Lesser Xing'an–Zhangguangcai Range	Cu–Zn–W	Medium	0.306	Biotite granite (173.6 ± 1.0) Granodiorite (173.9 ± 1.0)	SK	Ccp, Mol, Bn, Sp, Gn, Mag, Sch, Pyh, Py	Cal, Grt, Hd, Qtz	176.7 ± 5.9	[31]
Huanggang (12)	Southern Great Xing'an Range	Fe–Sn–W-Zn–Cu	Large	0.24	K-feldspar granite (136.7 ± 1.1) Granite porphyry (136.8 ± 0.57)	SI, HO, AL, SK, CH, EP, SE, CA	Mag, Cst, Vlm, Sch, Sp, Lö, Ccp, Mol, Bin, Pyh, Apy, Py	Grt, Hbl, Fl, Cal, Qtz, Ep, Chl, Act, Phl	135.31 ± 0.85	[32–34]
					Greisen-related quartz vein type					
Yangjingou (2)	The Yanbian Belt	W	Large	0.22 to 1.5	Granodiorite (249.4 ± 2.7)	SE, ACT, AL, CA, EP	Sch, Py, Gn, Apy, Pyh, Ccp	Qtz, Ms, Hbl, And, Ep, Act	230.79 ± 1.19	[23,35]
Baogeda Ula (16)	Northern side of the Erenhot–Hegenshan Fault	Mo–W	Medium	0.23	Porphyritic granite (240.9 ± 2.5)	KF, SI, SE, EP, CH	Wfm, Sch, Gn, Py, Ccp, Bn	Qtz, Ms, Fe-Ms, Bt, Kfs, Ser, Tpz, Tur, Fl	232.5 ± 3.2	[17,36]

Table 1. *Cont.*

Deposit (No. in Figure 1)	Location	Commodity	Size	Grade (WO₃, %)	Ore-Forming Intrusions (Ma)	Wall-Rock Alteration	Ore Mineral Assemblage	Gangue Mineral Assemblage	Ore-Forming Ages (Ma)	References
Wudaogou (3)	Eastern Yanbian Belt	W	Medium	0.66 to 3.53	Granodiorite (267.8 ± 1.0)	SI, AL, CH, EP, BI, MU	Sch, Mol, Py, Gn, Aot, Pyh, Ccp	Qtz, Cal, Ab, Act, Bt, Ser, Ap	-	[23,37]
Weilianhe (8)	Middle of the Great Xing'an Range	W	Small	-	Granite (145.4 ± 1.0)	KF, EP, CH, SI, SE, PY	Wof, Sch, Py	Qtz, Kfs, Ser, Bt, Hbl	-	[38,39]
Shamai (14)	The north of the Erenhot–Hegenshan Fault	W	Medium	0.36	Fine-grained monzogranite (142.5 ± 1.0) Medium-grained monzogranite (141.9 ± 1.1) Porphyritic monzogranite (140.2 ± 0.99)	GR, HO, MU, SE	Wfm, Mol, Py, Ccp, Bn, Apy, Gn, Sp	Fe-Ms, Qtz, Kfs, Ab, Ms, Tpz, Ilt, Bt, Fl	137 ± 2.0	This Paper
Dayana (15)	The north of the Erenhot–Hegenshan Fault	W–Mo	Small	0.81	Biotite granite (135 ± 1.0)	GR, SI, EP, MU, CH, KF, AL	Wfm, Mol, Sch, Ccp, Cu, Py, Sp	Ms, Qtz, Brl, Kfs, Ab, Fl	132 ± 1.0	[38,40]
Polymetallic W-Mo-Cu vein type										
Daolundaba (11)	Southern Great Xin'an Range	Cu–W–Sn	Medium	0.1 to 1	Fine- to medium-grained biotite monzogranite (292.1 ± 0.84)	SI, GR, FL, SE, CA, CH, KA, KF, TO	Pyh, Cst, Wfm, Ccp, Apy, Ttr, Sp, Gn, Py	Qtz, Fl, Kfs, Ser, Chl, Cal	282.7 to 290.0	[41,42]
Wurinitu (17)	Western part of the Erenhot–Dong Ujimqin metallogenic belt	Mo–W	Small	0.12	Monzonitic granite (137.3 ± 1.3) Granite porphyry (131.9 ± 1.5)	SK, SI, SE, EP, FL, PY, CA	Mol, Sch, Wfm, Ccp, Sp, Bin, Sbn, Gn	Qtz, Fsp, Ms, Ser, Fl, Bt	142.2 ± 2.5	[43,44]
Weilasituo (13)	Southern part of the Great Xing'an Range	Sn–Cu–W–Mo–Zn–Pb–Ag	Medium	0.14	Quartz porphyry (138 ± 2.0)	GR, SI, MU, FL	Cst, Wfm, Mol, Sp, Apy, Ccp, Ttr	Qtz, Fl, Ms, Cal	135 ± 11.0	[45]

Table 1. *Cont.*

Deposit (No. in Figure 1)	Location	Commodity	Size	Grade (WO$_3$, %)	Ore-Forming Intrusions (Ma)	Wall-Rock Alteration	Ore Mineral Assemblage	Gangue Mineral Assemblage	Ore-Forming Ages (Ma)	References
Chamuhan (18)	Western part of the Songliao Terrane	Mo–W	Small	1.875	Altered medium-grained monzogranite (144 ± 2) Fine-grained monzogranite (139 ± 2)	AL, GR, CH, SE	Wfm, Cst, Mol, Sch, Apy, Bin, Gn	Qtz, Fl, Tur, Mnz, Ms, Brl, Tpz	140 ± 2	[46]
					Porphyry type					
Honghuaerji (10)	Mid-northern part of the Great Xing'an Range	W–Mo	Large	0.315	Biotite granite (179.4 ± 2.3)	KF, AL, SE, GR, SI, CA	Sch, Wfm, Mol, Py, Ccp, Sp	Qtz, Fsp, Ser, Kln, Cal	176.8 ± 2.2	[11,12,38]
Dongshanwan (9)	Southern segment of the Great Xin'an Range	W–Mo	Small	0.2	Granite porphyry (151.4 ± 0.8)	KF, SI, SE, KA	Wfm, Sch, Apy, Cst, Sp, Gn, Py	Kfs, Qtz, Ser, Fl, Cal	149.3 to 155.4	[47]

Size: small sized (<10,000 t WO$_3$); medium sized (10,000 t to 50,000 t WO$_3$); large sized (>50,000 t WO$_3$). Alteration abbreviations: AC: actinolitization; AL: albitization; BI: biotitization; CA: carbonatation; CH: chloritization; EP: epidotization; FL: fluoritization; GR: greisenization; HO: hornfelization; KA: kaolinization; KF: K-feldspathization; Mu: muscovitization; PY: pyritization; SE: sericitization; SI: silicification; SK: skarnization; TO: tourmalinization. Mineral abbreviations: Act: actinolite; Ab: albite; And: andalusite; Ap: apatite; Apy: arsenopyrite; Aug: augite; Brl: beryl; Bn: bornite; Bin: bismuthinite; Bt: biotite; Cal: calcite; Cst: cassiterite; Ccp: chalcopyrite; Chl: chlorite; Cu: native copper; Di: diopside; Dol: dolomite; Ep: epidote; Fl: fluorite; Fe-Ms: ferrimuscovite; Fsp: feldspar; Gn: galena; Grt: garnet; Gro: grossularite; Hbl: hornblende; Hd: hedenbergite; Ilt: illite; Ilv: ilvaite; Lö: löllingite; Kln: kaolinite; Kfs: K-feldspar; Mag: magnetite; Mol: molybdenite; Mnz: monazite; Ms: muscovite; Phl: phlogopite; Pl: plagioclase; Py: pyrite; Pyh: pyrrhotite; Qtz: quartz; Sch: scheelite; Ser: sericite; Sp: sphalerite; Srp: serpentine; Sbn: stibnite; Ttr: tetrahedrite; Tpz: topaz; Tr: tremolite; Tur: tourmaline; Vlm: varlamoffite; Ves: vesuvianite; Wfm: wolframite.

2. Geological Background

2.1. Xing'an–Mongolia Orogenic Belt (XMOB)

Northeastern China (XMOB) is generally considered part of the CAOB, which lies between the Siberian and North China cratons (Figure 1a,b). As one of the largest Phanerozoic orogens in the world, the CAOB is a natural laboratory for studies of continental dynamics and metallogenesis [3]. The CAOB comprises a collage of massifs, terranes, fold belts, and ophiolite slices [48] and records the influence of a long-term accretionary orogenic and continental crust growth event relating to the Paleo-Asian Ocean [1,2,48–54].

The Xing'an–Mongolia Orogenic Belt (XMOB) is situated in the eastern segment of the CAOB, encompassing the central-eastern part of Inner Mongolia and the northeastern region of China (Figure 1b). The XMOB has four blocks and four sutures (Figure 1b), namely the Erguna, Xing'an–Airgin Sum (referred to as Xing'an in this study), Songliao–Hunshandake, and Jiamusi Blocks and the Xinlin–Xiguitu, Xilinho–Heihe, Mudanjiang, and Ondor Sum–Yongji sutures [55]. It underwent intense magmatic activity during the Late Paleozoic and Mesozoic eras, accompanied by extensive endogenous mineralization. Being a natural laboratory for studying orogenic belt evolution, it has consistently been a prominent subject in geological research [6].

The tectonic evolution of the XMOB has been the subject of intense debate (seen in [5]). There is disagreement on whether the Paleo-Asian Ocean closed during the Devonian or Early Mesozoic, as well as on whether the tectonic activities during the Carboniferous and Permian were driven by continuous subduction–arc systems or extension following the orogenic process. An alternative model for the orogenic history of Central Inner Mongolia was presented in [5], which includes (i) an Early Paleozoic trench–arc system (500~410 Ma); (ii) a Devonian collisional orogeny resulting from the closure of the Paleo-Asian Ocean (~400 Ma); (iii) extension events in the Carboniferous and Permian periods following the collision (350~250 Ma); and (iv) within-plate orogeny in the Early–Middle Triassic due to the closure of limited sea basins (~240 Ma). Xu et al. [7] introduced the concept of the "Xing-Meng Intracontinent Orogenic Belt" (XMIOB) after examining the Late Paleozoic to Early Mesozoic intra-continental extension and orogenic evolution of the XMIOB from the perspectives of tectonics, sedimentary formation, magmatism, and metamorphism. Xu et al. [6] provided a comprehensive overview of recent geological studies in the XMOB. The investigation reveals that the XMOB, influenced by Paleozoic orogenic processes, consists of microcontinental massifs and orogenic belts. The presence of Precambrian basement in the microcontinental massifs with crustal accretion occurring in the Neoproterozoic, Mesoproterozoic, Neoarchean, and Paleozoic was also noted. The study highlights the tectonic nature and processes from the Late Paleozoic to the Paleogene, including the transformation from active continental margin to trench–arc–basin system and the opening of the Japan Sea.

2.2. Shamai Tungsten Deposit

2.2.1. Regional Geology

The Shamai–Yuguzer tungsten (molybdenum) mineralization belt, situated in the eastern section of the China–Mongolia border (Figure 1b,c), is the largest tungsten–molybdenum belt in Northeast Asia and north of the Yangtze River of China in terms of production and reserves, presenting significant exploration potential [16]. Located within the XMOB and north of the Chagan'aobao–Wuchagou deep fault, it lies at the intersection of the southeastern margin of the Siberian Plate's Irtysh Paleozoic tectonic–magmatic belt and the southern segment of the Greater Khingan Range Mesozoic tectonic–magmatic belt.

The area's exposed strata include Middle Ordovician tuff, tuffaceous siltstone, fine sandstone, and bioclastic limestone; Upper Silurian slate, sandstone, and bioclastic lime-

stone; Devonian tuffaceous sandstone, mudstone, limestone, and slate; Upper Carboniferous to Lower Permian andesite and dacite with associated lavas and pyroclastic rocks; and Upper Permian to Jurassic tuffaceous sandstone, mudstone, and coal-bearing sedimentary rocks (Figure 1c). Quaternary deposits consist of sand, mud, and gravel.

The region is characterized by extensive fault structures, particularly northeast-trending faults, which not only define lithological boundaries but also serve as conduits for magma and ore-bearing fluids, as evidenced by the numerous tungsten and tungsten (molybdenum) anomalies and alteration zones along these faults. Paleozoic and Mesozoic granitoid intrusions, covering 70% of the exposed rock, are widespread and include Hercynian diorite and granodiorite, Indosinian–Yanshanian monzogranite, biotite granite, alkali-feldspar granite, and felsic dikes [16]. The Shamai biotite granite is particularly notable for its scale, high tungsten and molybdenum contents, and association with tungsten and tungsten (molybdenum) deposits (Figure 1c).

2.2.2. Ore Deposit Geology

The Shamai tungsten deposit (Figure 2) is located in the southwestern part of the Xing'an–Airgin Sum block to the north of the deep-seated Hegenshan Fault (Figure 1b) [56]. Magmatic rocks clearly reveal structural trends within the regional area in two directions: northeast (NE) and north-northeast (NNE). The Shamai tungsten deposit is hosted at the intersection of these two structural trends.
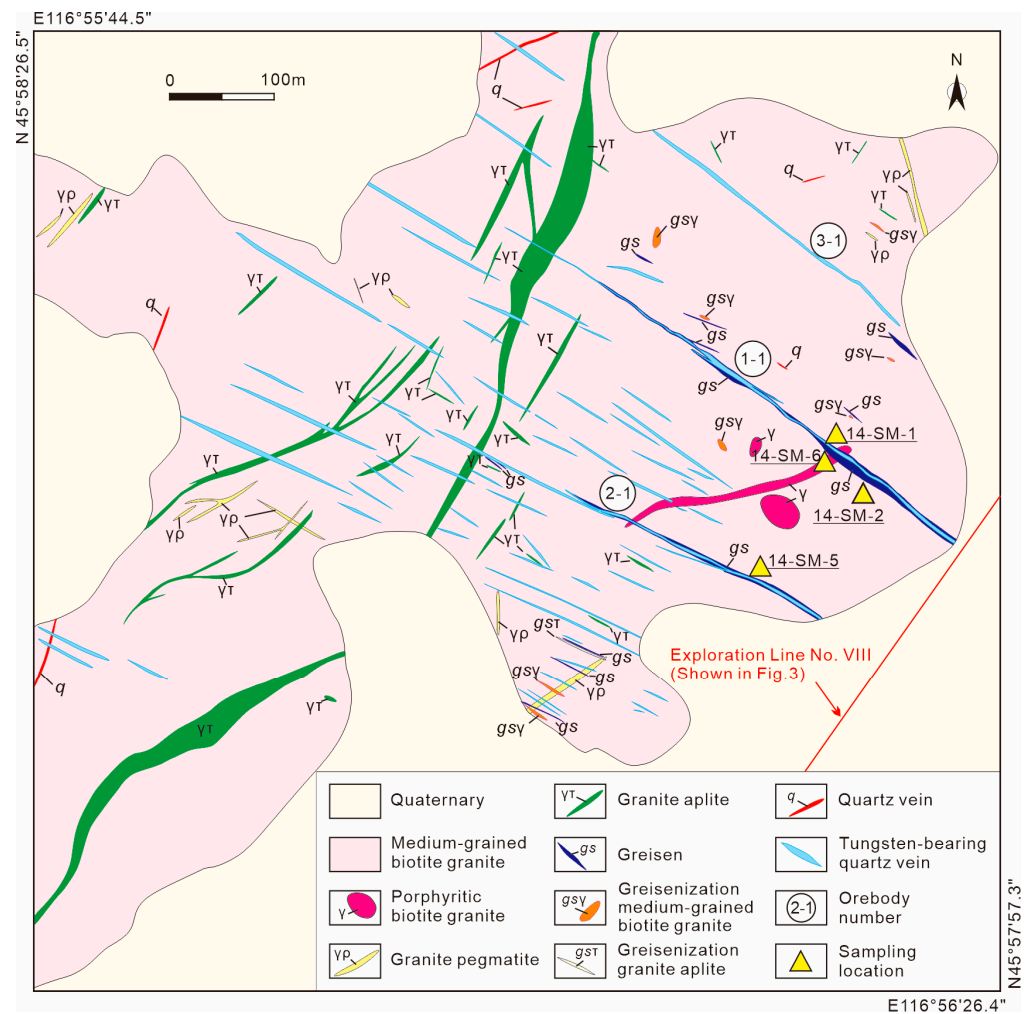
Figure 2. Simplified geological map of the Shamai tungsten deposit (modified from [18]).

The oldest formation in the block is the Middle Ordovician Hanwula Formation, which contains tuff, tuffaceous siltstone, siltstone, and fine sandstone units (Figure 1c). The block also has fine-grained clastic rocks of the late Silurian Barundele Formation, and sandstone, slate, tuff, and intermediate to basic volcanic rocks of the Devonian Ageryinwula Formation (Figure 3). This area also contains the Early Jurassic Manitemiao Formation (Figure 3), which comprises a lacustrine coal-bearing clastic sedimentary sequence, Late Jurassic intermediate to felsic lavas and pyroclastics, and Late Cretaceous limnic facies coal-bearing clastic rocks. The youngest Cenozoic sediments (Figures 2 and 3) in this region consist of a series of pelitic sandstone, mudstone, sandy conglomerate, clay, and aeolian sand units [15,55,57].
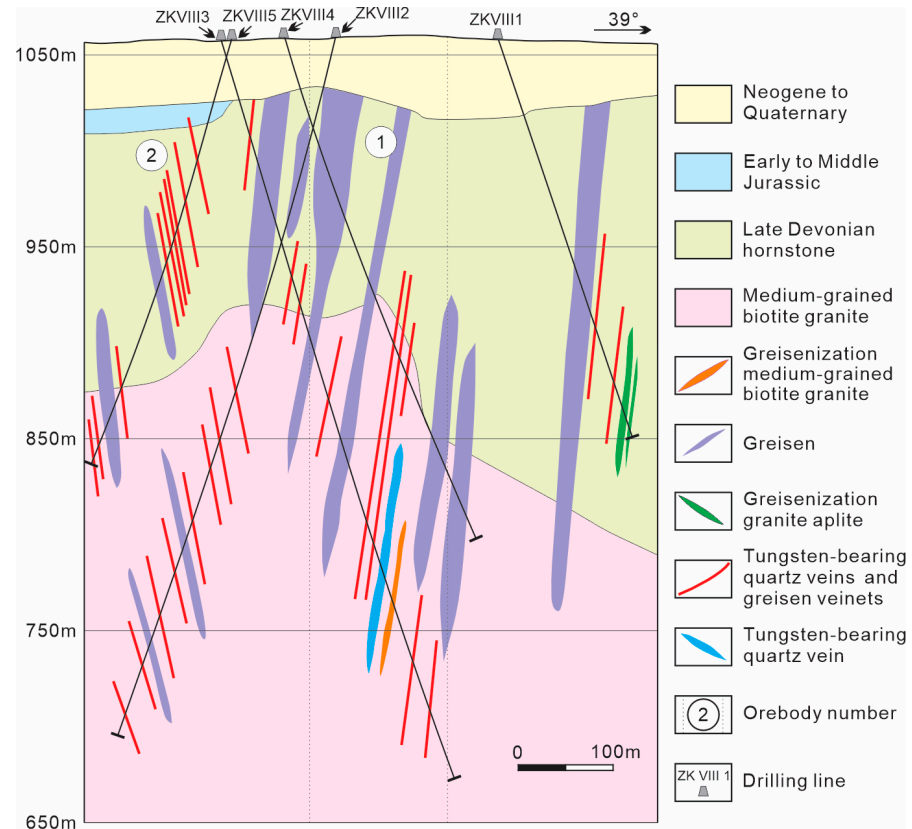
Figure 3. Cross-section of Exploration Line No. VIII through the Shamai mining area (modified from [15]).

The Shamai granite crops out over an area of 2500 km^2 and is the largest pluton in the region (Figures 1c and 2). This pluton was intruded into the Late Devonian and Jurassic units and is elongated in NNE–SSW direction, extending into Mongolia. It is associated with several W–Mo deposits (Figure 1c). The Shamai granite contains fine- to medium-grained biotite monzogranite, porphyritic biotite monzogranite, granitic pegmatite, and aplite phases (Figures 2, 3 and 4a–c). The pluton is dominated by the oldest fine- to medium-grained biotite monzogranite phase (Figures 2 and 4i), which contains microcline (25–30 vol.%), plagioclase (30–35 vol.%), quartz (25–35 vol.%), and biotite (5–10 vol.%), with accessory ilmenite, titanite, magnetite, zircon, apatite, and allanite (Figure 4a,b). Some microcline, plagioclase, and biotite have been replaced by flaky muscovite or sericite (Figure 4h). The porphyritic biotite monzogranite phase in the pluton contains phenocrysts of 3–10 mm in size (30–40 vol.%; Figure 4c) and is mineralogically similar to the fine- to medium-grained biotite monzogranite, with the boundary between the two phases being transitional in places. This suggests that these two granite phases were emplaced

contemporaneously. The younger granitic pegmatite and aplite dikes were emplaced along NW–SW or NE–SW trending fractures within the fine- to medium-grained biotite monzogranite and porphyritic biotite monzogranite (Figure 2).
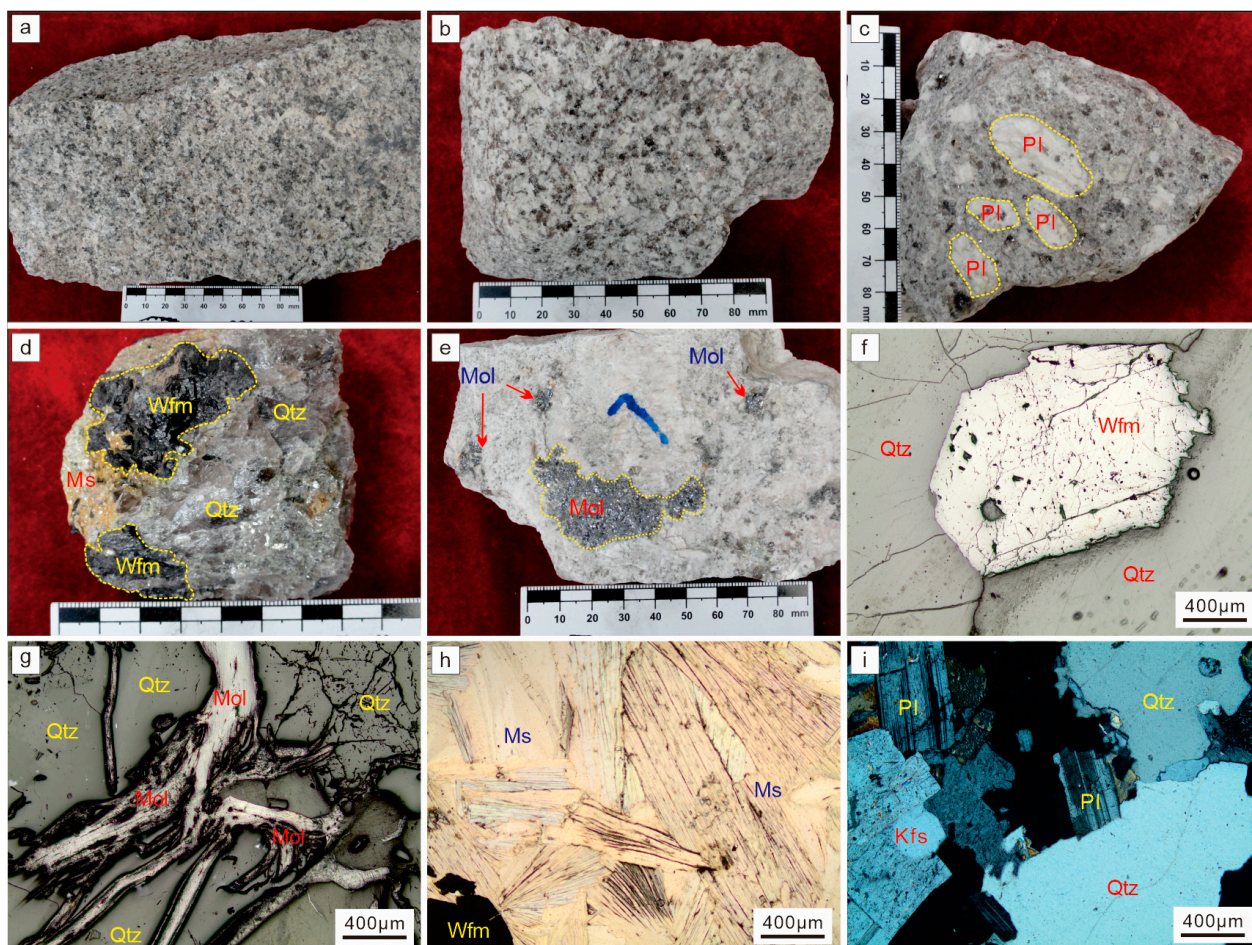
Figure 4. Photomicrographs of tungsten-bearing ore minerals and host rocks from the Shamai tungsten deposit: (**a**) fine-grained biotite monzogranite, (**b**) medium-grained biotite monzogranite, (**c**) porphyritic biotite monzogranite, (**d**) tungsten-bearing quartz vein, (**e**) disseminated molybdenite within a granitic aplite, (**f**) wolframite-bearing quartz vein, (**g**) molybdenite-bearing quartz vein, (**h**) muscovite and wolframite within a greisen-altered medium-grained biotite granite, and (**i**) fine- to medium-grained biotite monzogranite. Abbreviations are as follows: Qtz: quartz, Pl: plagioclase, Wfm: wolframite, Mol: molybdenite, and Ms: muscovite.

Tungsten mineralization primarily occurs in vein form within the Shamai granite intrusions and their surrounding rocks, with the ore bodies controlled by NW-trending transtensional faults in the mining area (Figure 2). These faults evolved from NW-trending shear joints developed within the granite body, serving both as the main structural framework of the mining area and as the primary ore-hosting structures. A total of 550 wolframite-bearing veins have been identified in the Shamai ore district, with seven considered economic. The veins define five ore zones that strike from 117°–297° to 127°–307° and are spaced some 110–138 m apart, with the No. 1, 2, and 3 orebodies containing the most economically significant mineralization within the deposit and extending to a depth of over 400 m (Figures 2 and 3) [15–18]. The deposit is divided into five vertical zones, from a basal veinlet zone upwards to zones containing thick veins, mixed thick veins, and veinlets and an uppermost zone containing very thin so-called thread veins (Figure 3). The deposit also contains both quartz-vein-hosted and greisen-type wolframite mineralization (Figures 2 and 3), with the

former having higher grades (0.23%–4.82% WO$_3$) than the latter (0.11%–0.77% WO$_3$). The quartz-vein-hosted ores consist of quartz and anhedral to euhedral wolframite (Figure 4d–f), with associated muscovite, fluorite, and topaz, whereas the greisen-type mineralization contains quartz and muscovite with minor amounts of disseminated fine-grained wolframite and associated fluorite (Figure 4e–i).

The Shamai deposit is associated with well-developed alteration that includes muscovite-, greisen-, and hornfels-type alterations, with the latter two strongly associated with tungsten mineralization (Figure 3). The muscovite and sericite alterations within the deposit represent the earliest stages of alteration and almost completely replace the magmatic biotite and feldspar within the intrusive rocks in this region. This muscovite alteration is overprinted by greisen alteration within the monzogranite, forming an assemblage containing quartz of 1–4 mm in diameter (50–75 vol.%), muscovite (25–50 vol.%), and minor wolframite. These greisen rocks are always located on the external sides of wolframite-bearing quartz veins (Figure 4), extending inward from greisen zones to strongly silicified greisen and muscovite-rich greisen zones [18].

Within the Shamai tungsten deposit, there are four stages of mineralization: silicate, oxide, sulfide, and fluorite. The paragenetic sequence of minerals is detailed in [18]. The silicate mineralization stage is subdivided into early and late greisen–silicate substages. The early greisen–silicate substage is associated with a wolframite, ferrimuscovite, quartz, K-feldspar, and albite assemblage. In contrast, the late greisen–silicate sub-stage is characterized by a wolframite, muscovite, topaz, illite, and quartz assemblage that fills fractures within the early greisen substage and associated host rocks. The oxide stage is related to the formation of the majority of the mineralization within the deposit and generated wolframite-bearing quartz veins hosted by faults and fractures. Pegmatites commonly host the veins and contain medium- to coarse-grained wolframite and topaz with accessory muscovite, biotite, illite, and quartz. The mineralization of the sulfide stage has less wolframite. It is characterized by molybdenite, pyrite, chalcopyrite, bornite, arsenopyrite, galena, and sphalerite that occur as veinlets or disseminated throughout the rock mass. The final fluorite stage is associated with developing fluorite–quartz veins that are commonly 30–50 mm wide, are only slightly enriched in tungsten, and crosscut the mineralization of the preceding stages [18].

3. Sampling and Analytical Methods

3.1. Sample Preparation

Samples were collected from the fine- to medium-grained biotite monzogranite and porphyritic biotite monzogranite phases of the intrusion associated with the Shamai deposit. The granitoid samples in the mining area, especially around the orebodies, have undergone muscovite and greisen alterations. Consequently, this study focuses on the least-altered samples, which were subjected to whole-rock major and trace element geochemical, zircon LA–ICP–MS U–Pb, and in situ zircon Hf isotopic analyses (sampling locations are shown in Figure 2). The samples subjected to in situ plagioclase Pb isotopic analysis were taken from the porphyritic biotite monzogranite, and the plagioclase that was analyzed was 12 mm long and 10 mm wide.

3.2. Analytical Methods

Whole-rock major element concentrations were determined using a PANanalytical Axios-advance PW4400 X-ray fluorescence (XRF) spectrometer at ALS, Guangzhou, China. Whole-rock trace element compositions were determined using ICP–optical emission spectrometry (ICP–OES) and ICP–MS, also at ALS. Triplicate analyses were reproducible within <5% for all elements, and the analysis of the OU-6 and GBPG-1 standards returned values consistent with their recommended compositions.

Before U–Pb dating, zircons were separated from samples 14-SM-1, 14-SM-2, and 14-SM-6 using conventional heavy liquid and magnetic techniques. The resulting zircon separates were examined under transmitted and reflected light and via cathodoluminescence (CL) at YuJin Technology, Chongqing, China, to image their external and internal structures. Selected zircons were dated using LA–ICP–MS employing an Agilent 7500a ICP–MS instrument(Agilent Technologies Co. Ltd, Beijing, Cina) equipped with a 193 nm excimer laser at the State Key Laboratory of Geological Processes and Mineral Resources, China University of Geosciences, Beijing, China. The 91,500 and Qinghu standard zircons were also analyzed, and a NIST 610 standard was used for optimization. These analyses employed a spot diameter of 36 μm, and all grain mounts were washed in dilute HNO_3 and pure alcohol before analysis to remove any potential lead contamination. Liu et al. [58] give details of the analytical methodology. Common Pb was corrected according to [59]. The resulting data were processed using the GLITTER and ISOPLOT programs [60], with uncertainties on individual analyses quoted at the 95% (1σ) confidence level.

In situ zircon Lu–Hf isotopic analysis was undertaken using a Neptune Plus multi-collector (MC)–ICP–MS equipped with a RESOlution M-50 laser ablation system (Applied Spectra, Sacramento, USA) at the State Key Laboratory of Isotopic Geochemistry, Guangzhou Institute of Geochemistry, Chinese Academy of Sciences, Guangzhou, China. All Lu–Hf isotopic measurements were undertaken on spots previously used for U–Pb analysis. The Lu–Hf analyses used a 45 μm spot size, a repetition rate of 8 Hz, and a laser energy setting of 80 mJ. Helium was used as a carrier gas, and a small amount of nitrogen was added to the gas line to enhance the sample signal. Single spot analyses consisted of 30 s of gas blank collection and 30 s of laser ablation data collection with an integration time of 0.131 s, yielding around 200 data collection cycles per analysis. ^{173}Yb and ^{175}Lu were used to correct the isobaric interferences of ^{176}Yb and ^{176}Lu on ^{176}Hf, and $^{176}Hf/^{177}Hf$ ratios were normalized to $^{179}Hf/^{177}Hf = 0.7325$ using an exponential law for mass bias correction. Xu et al. [61] and Wu et al. [62] detail the analytical techniques used, and a Penglai standard zircon was analyzed as a standard.

In situ plagioclase Pb–Pb isotopic analyses were undertaken using a Neptune plus MC–ICP–MS instrument equipped with a 193 nm RESOlution M-50 LA system. These analyses used a 45 μm laser spot size, a laser energy of 80 mJ, an attenuate value of 25%, a repetition rate of 3 Hz, and an integration time of 0.262 s. They were undertaken at the State Key Laboratory of Isotopic Geochemistry, Guangzhou Institute of Geochemistry, Chinese Academy of Sciences, Guangzhou, China. NIST 612 and GSD-1G standard glasses were also analyzed. Zhang et al. [63] give details of the analytical techniques.

4. Results

4.1. Major and Trace Elements

The whole-rock major and trace element compositions of the samples from the study area are given in Supplementary Table S1. The fine- to medium-grained biotite monzogranite samples contain 74.21–76.10 wt% SiO_2, 12.86–14.60 wt% Al_2O_3, 3.25–4.66 wt% Na_2O, 2.68–5.06 wt% K_2O, and 0.04–0.11 wt% MgO and are classified as peraluminous. In comparison, the porphyritic biotite monzogranite samples have similar compositions and contain 72.21–75.32 wt% SiO_2, 4.67–7.53 wt% K_2O, and 13.06–14.22 wt% Al_2O_3.

All the samples from the study area have chondrite-normalized rare earth element (REE) diagram patterns (Figure 5a–d) that are slightly enriched in the light REE (LREE), have flat, heavy REE (HREE) patterns, and record moderate fractionation of the LREE from the HREE, with $(La/Yb)_N$ values of 1.34–12.66. These samples also have negative Eu anomalies with Eu/Eu^* ratios of 0.02–0.21. The primitive-mantle-normalized multi-element variation diagram patterns for these samples are characterized by enrichments in large ion lithophile elements (LILE; e.g., Rb, Th, and U) and depletions in Ba, Sr, P, Ti, and Nb.
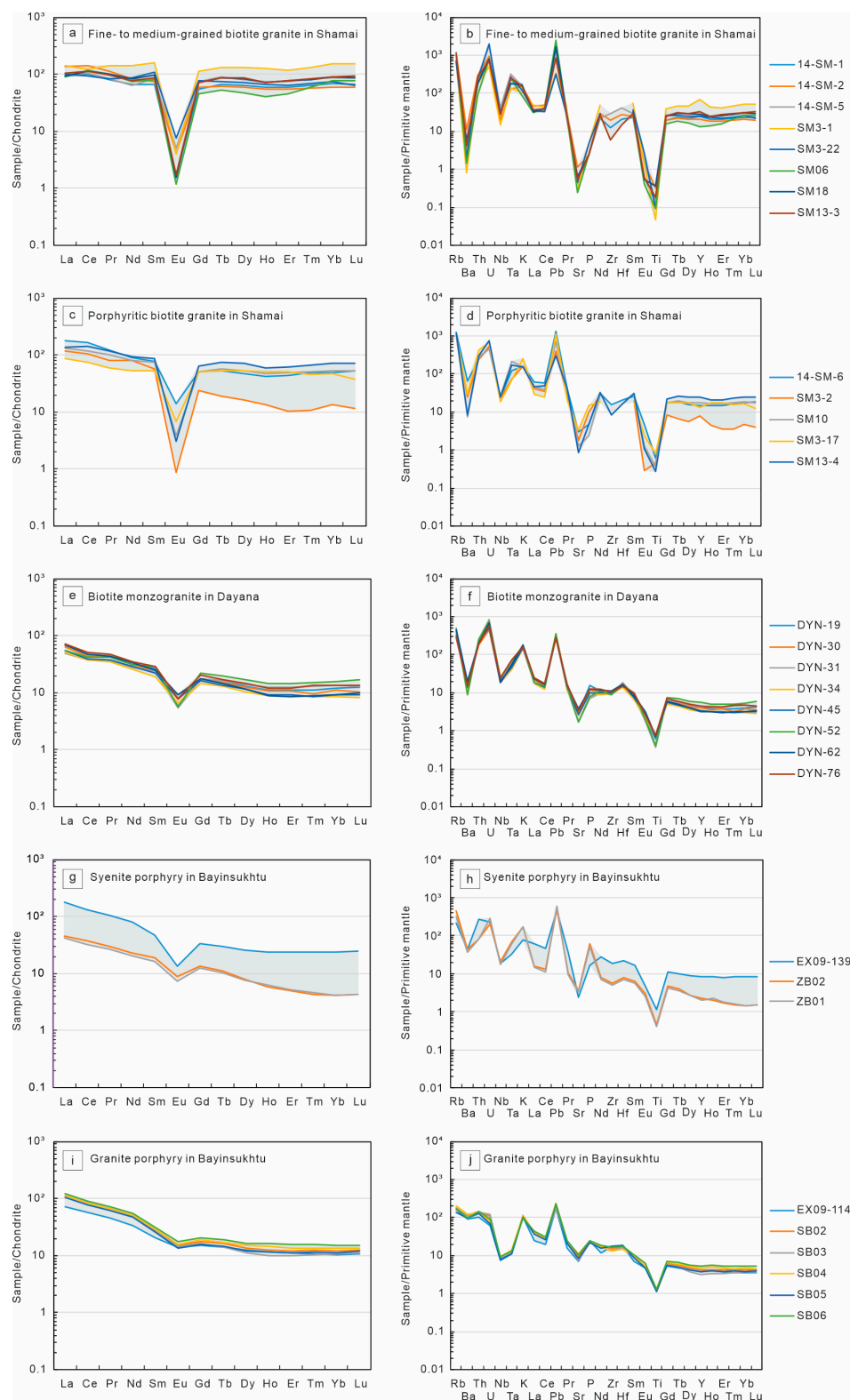
Figure 5. Chondrite-normalized REE (**a,c,e,g,i**) (normalized to the chondrite composition of [64]) and primitive-mantle-normalized multi-elements (**b,d,f,h,j**) (normalized to the primitive mantle composition of Sun and McDonough's [64] variation diagrams for the igneous rocks from the Shamai, Dayana, and Bayinsukhtu tungsten deposits. Data for the Shamai deposit are from this paper and [18], shown in Supplemental Table S1. Data for the Dayana deposit are from [38]. Data for granite porphyry from the Bayinsukhtu deposit are from [22]. Data for syenite porphyry from the Bayinsukhtu deposit are from [65].

4.2. Zircon CL Imaging and U–Pb Data

Zircons from the Shamai tungsten deposit are euhedral–subhedral, prismatic, colorless, transparent, and 100–300 μm long. The CL imaging of zircons indicates they contain clear micro-scale oscillatory zoning (Figure 6), suggesting a magmatic origin, supported by their high Th/U ratios (0.20–0.64). These zircons do not exhibit overgrowth rims or inherited cores. The magmatic characteristics of these zircons indicate that their U–Pb ages correspond to the timing of crystallization of the intrusions. The zircon LA–ICP–MS U–Pb dating results are in Supplementary Table S2 and Figure 7. Eighteen zircons yielded a weighted mean $^{206}Pb/^{238}U$ age of 142.5 ± 1.0 Ma (2σ; 95% confidence interval) for the fine-grained biotite monzogranite. A further fifteen zircons yielded a weighted mean $^{206}Pb/^{238}U$ age of 141.9 ± 1.1 Ma (2σ) for the medium-grained biotite monzogranite phase of the pluton. Finally, twenty-four zircons from the porphyritic biotite monzogranite yielded a weighted mean $^{206}Pb/^{238}U$ age of 140.2 ± 0.99 Ma (MSWD = 0.64; 95% confidence interval). These ages represent the timing of the crystallization phases of the pluton.
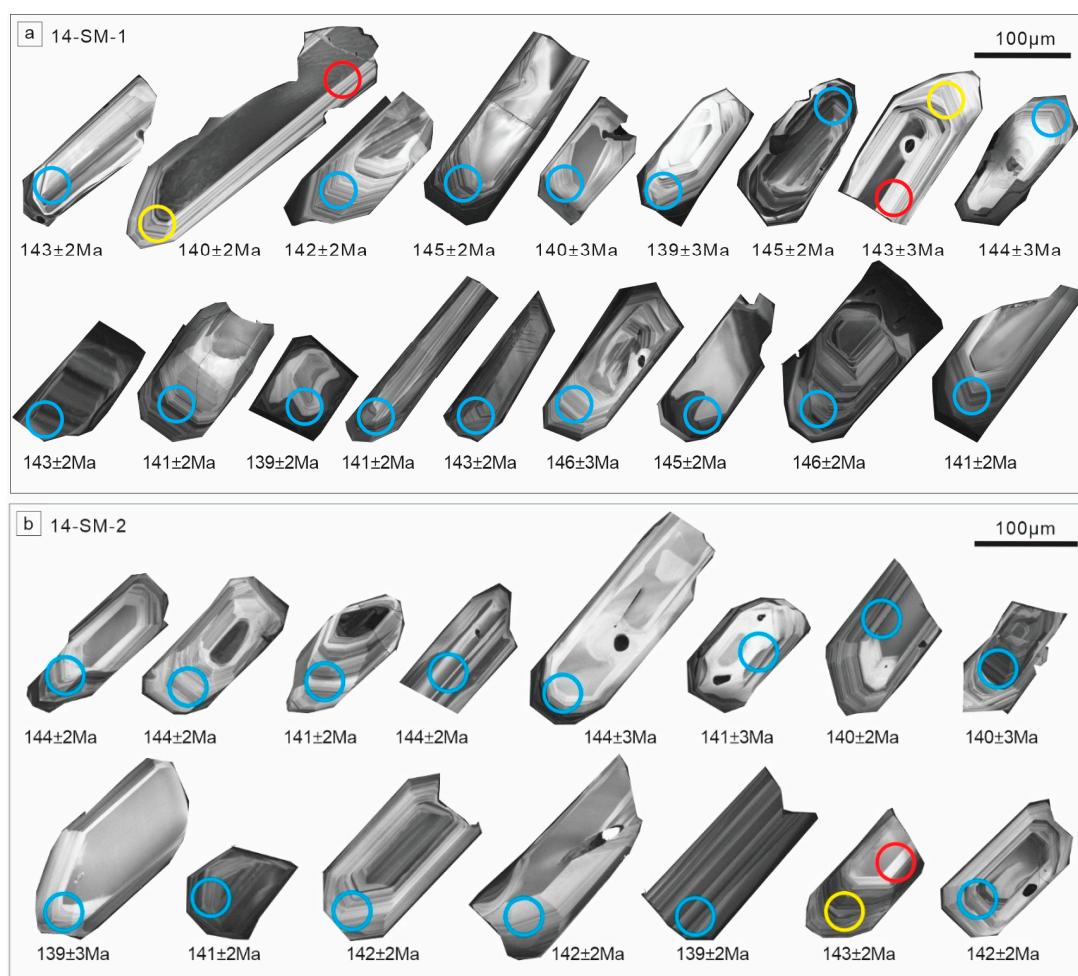
Figure 6. *Cont.*
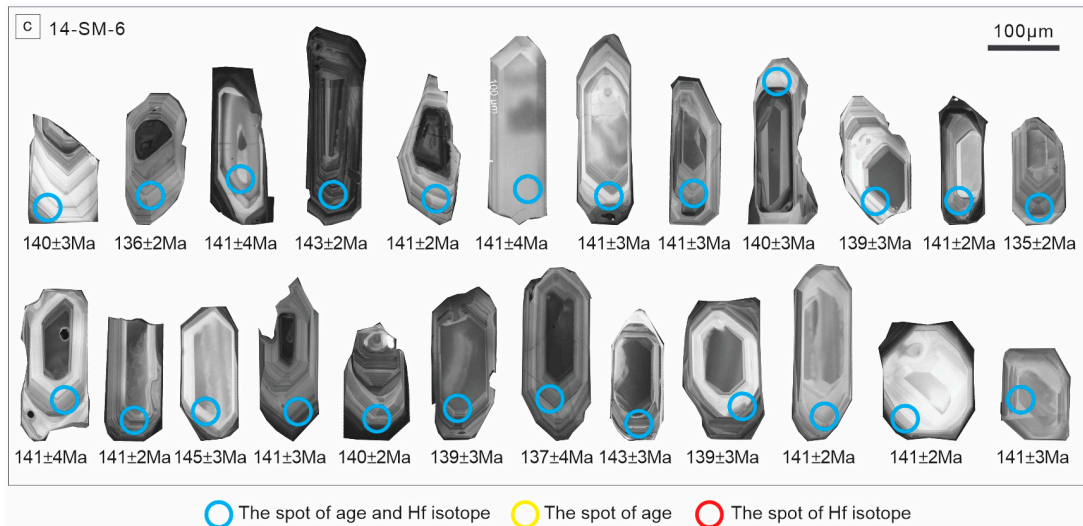
Figure 6. Representative cathodoluminescence images of zircons from (**a**) fine-grained biotite monzogranite sample 14-SM-1, (**b**)medium-grained biotite monzogranite sample 14-SM-2, and (**c**) porphyritic biotite monzogranite sample 14-SM-6 from the Shamai tungsten deposit.
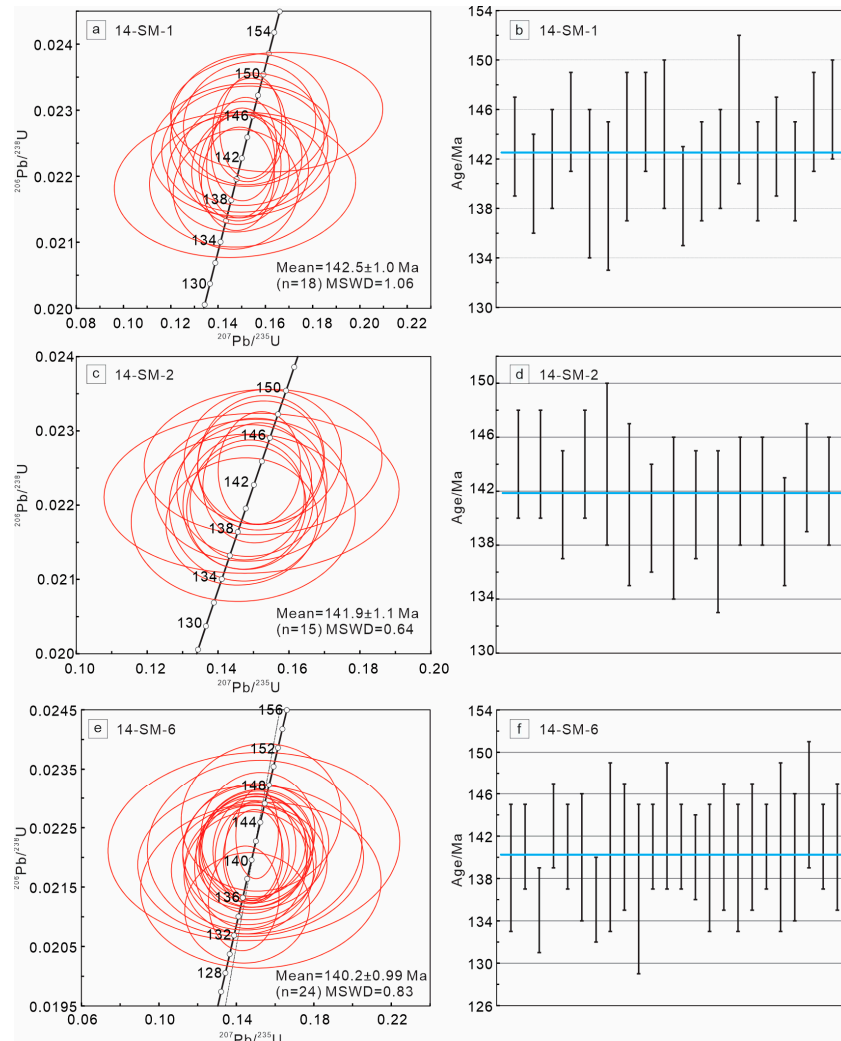
Figure 7. U–Pb concordia diagrams and age histograms for zircons from fine-grained biotite monzogranite sample 14-SM-1 (**a**,**b**), medium-grained biotite monzogranite sample 14-SM-2 (**c**,**d**), and porphyritic biotite monzogranite sample 14-SM-6 (**e**,**f**) from the Shamai tungsten deposit.

4.3. In Situ Zircon Hf Isotopes

Some zircon LA–ICP–MS analysis spots used for U–Pb dating were also used for in situ Hf isotopic analysis (Figure 6; Supplementary Table S3). A total of 17 spot analyses were obtained for the fine-grained biotite monzogranite sample, yielding variable $\varepsilon_{Hf}(t)$ values between 3.2 and 7.4 with T_{DM2} ages of 996–722 Ma and initial $^{176}Hf/^{177}Hf$ ratios of 0.282783–0.282899. A further 15 spot analyses were undertaken on zircon from the medium-grained biotite monzogranite sample, yielding negative $\varepsilon_{Hf}(t)$ values (–4.3 to –7.9), T_{DM2} model ages of 922–692 Ma, and initial $^{176}Hf/^{177}Hf$ ratios of 0.282809–0.282911. Finally, 19 spot analyses of zircons from the porphyritic biotite monzogranite yielded variable $\varepsilon_{Hf}(t)$ values between 4.2 and 7.6 with T_{DM2} ages of 923–728 Ma and initial $^{176}Hf/^{177}Hf$ ratios of 0.282810–0.282904.

4.4. In Situ Plagioclase Pb Isotopic Analysis

The spots used for in situ Pb isotopic analyses of plagioclase are shown in Figure 8, and the resulting lead isotopic compositions are listed in Supplementary Table S4. This plagioclase yields $^{206}Pb/^{204}Pb$ values of 18.373–18.536, $^{207}Pb/^{204}Pb$ values of 15.485–15.661, and $^{208}Pb/^{204}Pb$ values of 37.976–38.259.
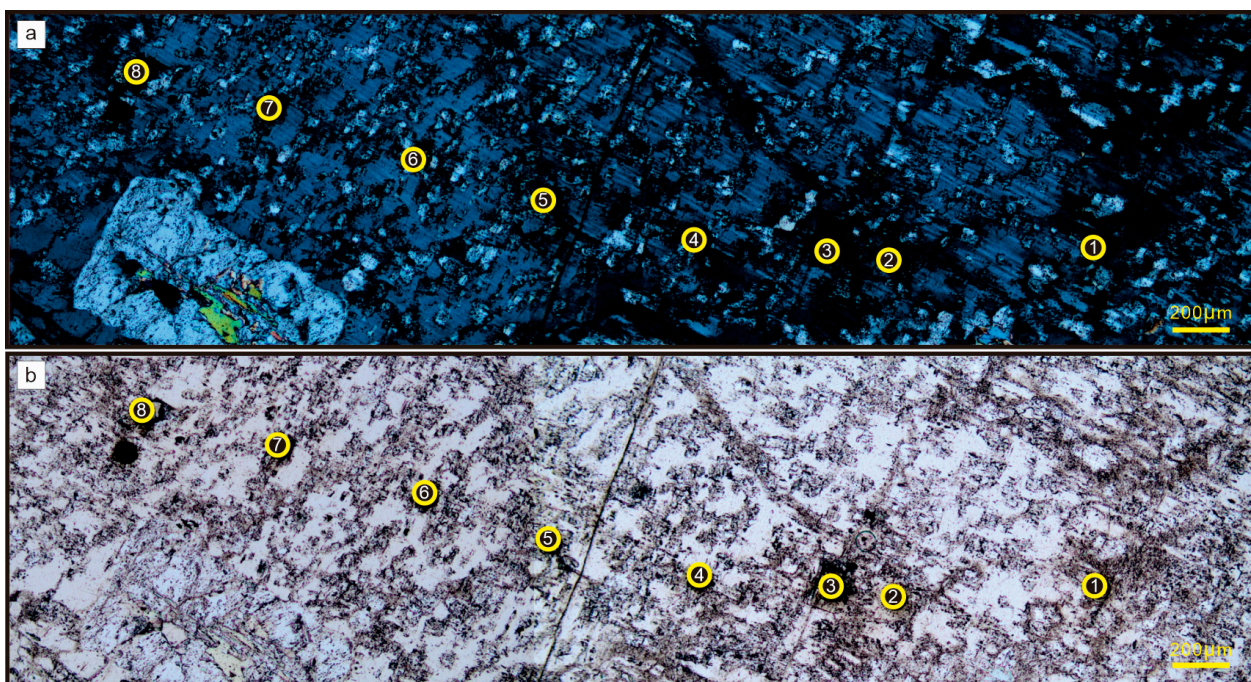
Figure 8. Sites of in situ Pb isotopic analysis of plagioclase within a porphyritic biotite monzogranite, shown under (**a**) cross-polarized and (**b**) plane-polarized light.

5. Discussion

5.1. Implications of the Shamai Deposit Mineralization for Tungsten Metallogeny in the Xing'an Block

The Xing'an Block is situated between the Hegenshan–Heihe and Tayuan–Xiguitu suture zones, adjacent to the Erguna Block and Songnen–Zhangguangcai Range block (Figure 1b). It primarily consists of Paleozoic–Mesozoic magmatic rocks and associated volcanic–sedimentary strata, with magmatic rocks mainly formed in the Early Paleozoic, Carboniferous–Permian, Late Triassic–Middle Jurassic, and Early Cretaceous periods [66]. The Erguna Block and Xing'an Block amalgamation occurred in the Early Paleozoic era, while the Xing'an Block and Songnen Block merged in the Late Carboniferous period [6]. Tungsten deposits in the Xing'an Block are mainly concentrated in the western section

(Figure 1b,c), including Shamai, Dayana, Yuguzier (Mongolia), Bayinsukhtu (Mongolia), Wurinitu, Baogeda Ula, and other locations. In contrast, smaller deposits like Weilianhe are found in the eastern section.

Various studies with different results have dated the Shamai tungsten deposit: Nie and Jiang [17] obtained a SHRIMP U–Pb age of 226 ± 1.5 Ma for a biotite granite in the region and a molybdenite Re–Os age of 224 ± 6 Ma. More recent dating efforts include determining a quartz-vein-hosted muscovite Ar–Ar plateau age of 140 ± 1 Ma, a molybdenite Re–Os model age of 137 ± 2 Ma, and zircon LA–ICP–MS U–Pb ages for fine- to medium-grained biotite monzogranite (153 ± 1 Ma) and porphyritic biotite monzogranite (146 ± 1 Ma) phases of the pluton [18]. Li et al. [67] also reported a wolframite Sm–Nd age of 137.9 ± 1.7 Ma for the Shamai deposit. Through zircon U–Pb isotopic analyses, we determined the weighted average ages of the fine-grained biotite monzogranite, medium-grained biotite monzogranite, and porphyritic biotite monzogranite in the Shamai deposit to be 142.5 ± 1.0 Ma (MSWD = 1.06), 141.9 ± 1.1 Ma (MSWD = 0.64), and 140.2 ± 0.99 Ma (MSWD = 0.64), respectively, representing their crystallization age as intrusive rocks. Finally, the Dayana W–Mo deposit associated with the Shamai–Yuguzer Granite yielded consistent zircon ages at approximately 134.2 ± 0.51 Ma and 134.6 ± 0.44 Ma for an associated biotite granite, as well as a molybdenite Re–Os isochron age of 132.9 ± 2.60 Ma [40]. Based on the available data, a significant tungsten metallogenic event occurred during the Early Cretaceous period in the western Xing'an Block (mineralization ages for other tungsten deposits are listed in Table 1). However, some small tungsten deposits, such as Bayinsukhtu [22], are still found in the Hercynian period.

Most primary tungsten mineralization is spatially associated with felsic magmatic rocks, commonly considered the source of these metals [68–70]. Yang [71] studied the age data of intrusive rocks in the Dong Ujimqin Banner area (where the Shamai tungsten deposit is located) and determined that granitic intrusion is the predominant rock type, with sporadic occurrences of mafic–ultramafic rocks. These intrusions primarily belong to the Hercynian and Yanshanian periods, with a minor contribution from the Indosinian. Among them, the Hercynian intrusions, including granite, diorite, and syenogranite, are most abundant and range in age from 277 Ma to 337 Ma. In contrast, the zircon ages of granitic rocks from the Yanshanian range from 130 Ma to 139 Ma. In addition to analyzing the geochemical data of the Shamai tungsten deposit in this study, we have also gathered geochemical data from the adjacent areas of the Dayana and Bayinsukhtu tungsten deposits (as shown in Figure 5) to investigate the relationship between felsic intrusions and tungsten mineralization in the western section of the Xing'an Block.

These samples are classified as the subalkalic series (Figure 9). However, there are differences between the Hercynian and Yanshanian intrusions regarding other geochemical characteristics, as indicated in Figures 5 and 9. For instance, the granite porphyry in the Bayinsukhtu tungsten deposit belongs to the medium K calc-alkaline series in the K_2O vs. SiO_2 diagram (Figure 9a). It exhibits a metaluminous characteristic in the A/NK vs. A/CNK diagram (Figure 9b). This type of granite was formed during the Late Carboniferous, as reported in [22]. The quartz diorite in the Dayana deposit shows similar geochemical characteristics and was also formed during the Late Carboniferous to Early Permian [71]. The samples from the granite porphyry in the Bayinsukhtu tungsten deposit (Figure 5i) differ from the Yanshanian granite on the chondrite-normalized REE diagram. They are enriched in LREE and do not exhibit any significant negative Eu anomalies. On the primitive-mantle-normalized trace element spidergram, these samples are slightly enriched in LILEs and slightly depleted in HFSE and P (Figure 5j). In contrast, the samples from Yanshanian, such as the mineralization-related fine- to medium-grained biotite monzogranite and porphyritic biotite monzogranite intrusions in the Shamai area, are medium- to high-K

calc-alkaline in the K_2O vs. SiO_2 diagram (Figure 9a) and show slight to strong peraluminous characteristics in the A/NK vs. A/CNK diagram (Figure 9b). The biotite granite has relatively low total REE values and has an LREE-enriched but flat HREE chondrite-normalized REE pattern with moderate LREE/HREE fractionation (Figure 5). The granite exhibits significantly negative Eu anomalies with δEu values ranging from 0.02 to 0.21 (Figure 5), suggesting the involvement of residual plagioclase in the petrogenesis of these granites. The biotite granite is enriched in LILE (e.g., Rb, Th, U, Nd, and Hf) but depleted in Ba, Sr, P, Ti, and Nb. This composition is similar to intrusions associated with tungsten deposits in southern China, indicating granites derived from crustal sources [72–74].
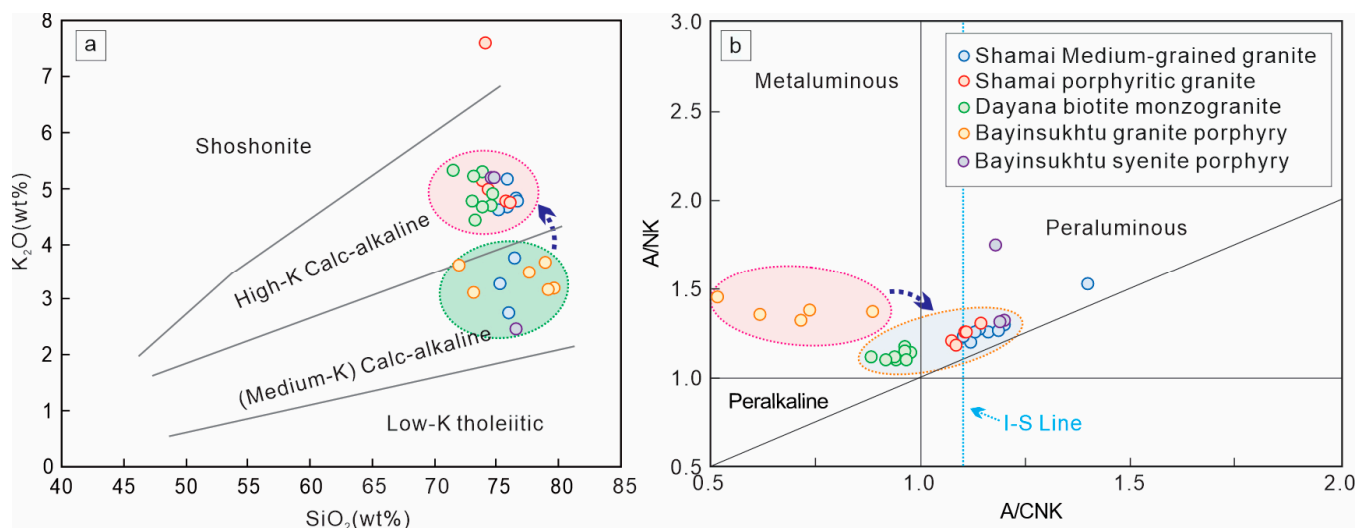
Figure 9. Plots of (**a**) K_2O vs. SiO_2 [75] and (**b**) A/CNK (i.e., Al_2O_3/CaO + Na_2O + K_2O) vs. A/NK (i.e., Al_2O_3/Na_2O + K_2O; [76]) for samples from the study area. Data sources are the same as for Figure 5. The I-S Line (A/CNK = 1.1) meets the criteria of [77,78].

The formation of tungsten mineralization is believed to be influenced by several processes, including cooling [79–81], reduced pressure [79,82], water–rock interaction [83,84], boiling and/or CO_2 effervescence [85–87], and mixing or dilution between magmatic and meteoric fluids [88,89]. Previous research on fluid inclusions from the Shamai tungsten deposit revealed that homogenization temperatures ranged from 260 °C to 320 °C, and salinities ranged from 5.11% to 8.81% NaCleqv [15]. Hu et al. [90] examined the fluid inclusions in quartz from tungsten-bearing quartz veins and greisens, identifying an H_2O-NaCl-CO_2 ± CH_4 fluid system. Moreover, the oxygen and hydrogen isotopic compositions of these inclusions suggest that the ore-forming fluids had $\delta^{18}O$ values ranging from 0.4‰ to 1.9‰ and δDw values ranging from −78‰ to −102‰. Most data are plotted between the magmatic water field and the meteoric water line in a δDw vs. $\delta^{18}Ow$ diagram (Figure 10). Previous data compiled from studies by Hu et al. [90] and Li and Xie [91] indicate that the fluid underwent an evolutionary trend from magmatic water to a mix of meteoric water during the transition from the greisenized topaz stage to the quartz stage and further to the W-bearing quartz vein mineralization stage, as shown in Figure 10. This confirms that these fluid inclusions reveal a significant influx of meteoric water into the system. The H-O isotopes provide evidence that the mixing of magmatic and meteoric fluids contributed to the precipitation of ore minerals during the formation of the Shamai deposit.
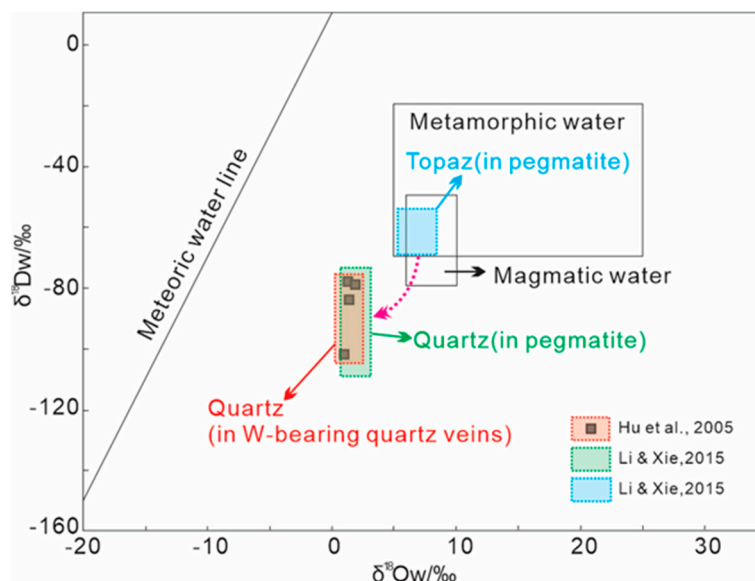
Figure 10. $\delta^{18}O$ versus δD diagram for ore-forming fluids associated with the Shamai tungsten deposit [15,91].

5.2. The Temporal and Spatial Patterns of Tungsten Mineralization in the XMOB

The Central Asian Metallogenic Domain holds valuable mineral resources, including porphyry-type, massive sulfide-type, magmatic Cu–Ni sulfide-type, and orogenic gold deposits [3]. The domain can be divided into three metallogenic provinces: the Kazakhstan copper–gold–molybdenum metallogenic province, the Mongolian copper–gold metallogenic province, and the northeast China (XMOB) molybdenum–copper polymetallic metallogenic province. Each province has its own unique geological and metallogenic characteristics. The northeast China (XMOB) metallogenic province has an extensive record of magmatic activity during the Meso-Neoproterozoic and Pan-African events, and porphyry molybdenum metallogenesis was prevalent during the Mesozoic. Jiang et al. [8] summarized previous research results and categorized ore deposits based on their relationship with different tectonic systems in the XMOB. They identified four categories of ore deposits based on their formation relative to specific tectonic systems and periods. These categories are ore deposits related to the Paleo-Asian Ocean, Mongol-Okhotsk Ocean, Paleo-Pacific, and the superimposition of the Mongol-Okhotsk Ocean and Paleo-Pacific tectonic systems. Lü et al. [92] examined the spatial–temporal distribution and tectonic settings of magma-to-hydrothermal ore deposits in the eastern CAOB. They suggested that the mineralizing event in this region began in the Cambrian, identifying six metallogenic stages at 510–473, 373–330, 320–253, 250–210, 210–167, and 155–100 Ma to date (Figure 11a).

Based on the latest published literature and including the Shamai deposit from this study, we have compiled key mineralization information for a total of 18 tungsten deposits (shown in Figure 1b) in the XMOB. After summarizing and analyzing these data, we found that the main mineralization types of these tungsten polymetallic deposits are primarily magmatic–hydrothermal (shown in Table 1), including skarn type (6), quartz vein type (6), hydrothermal vein type (4), and porphyry type (2). The overall mineralization ages range from 520 Ma to 132 Ma (Figure 11a). From a regional distribution perspective, the Erguna–Xing'an Block has the highest concentration of deposits, mainly consisting of independent tungsten deposits, while tungsten deposits in other terranes are mostly of the associated type. These characteristics indicate that the temporal and spatial evolution of tungsten mineralization in the XMOB region is not evenly distributed but rather shows specific concentrated areas in terms of mineralization timing and spatial distribution.
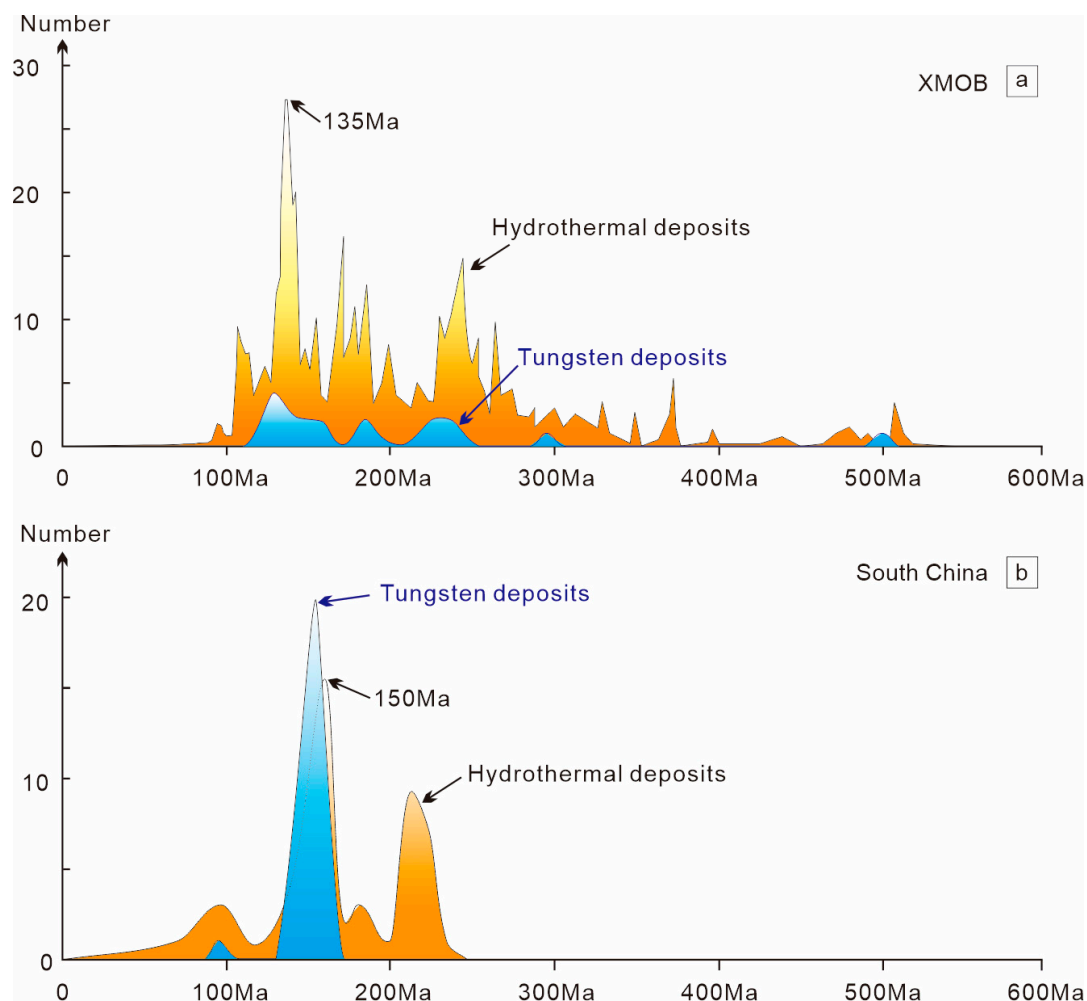
Figure 11. Timing of tungsten mineralization in NE China compared with the timing of tungsten mineralization within the South China and the magmatic–hydrothermal mineralization within the eastern CAOB. The tungsten mineralization ages for the XMOB are shown in Table 1. The magmatic–hydrothermal mineralization ages for the eastern CAOB are from [92]. The hydrothermal mineralization age for South China is from [93]. The tungsten mineralization ages for the South China are from [94].

From a temporal evolution perspective, by comparing the magmatic–hydrothermal ore deposits in the XMOB with the tungsten mineralization evolution in South China (Figures 11 and 12), it can be observed that tungsten mineralization occurred in the XMOB to varying degrees from the Paleozoic to the Mesozoic era, with notably lower intensity in the Paleozoic than in the Mesozoic. Moreover, tungsten mineralization in the XMOB is concentrated in the Mesozoic era, showing a trend of increasing quantity, diversity, intensity, and scale. However, compared to the tungsten deposits in South China, the mineralization age in the XMOB is notably less concentrated, the mineralization intensity is much lower, and the deposit scales are smaller. The key factors for tungsten mineralization in South China mainly include large-scale Mesozoic magmatic activity. These granites typically have high volatile content (such as F), and the Jurassic tungsten-mineralized granites in the Nanling region primarily formed due to the rollback of the Pacific plate [95]. The Late Cretaceous tungsten mineralization in the southern region is related to the rollback of the Neo-Tethys Ocean [9,95]. These factors, particularly the large-scale activity of highly differentiated granites and the spatiotemporal coupling of plate rollback, do not exhibit high spatiotemporal concentration in the XMOB region.
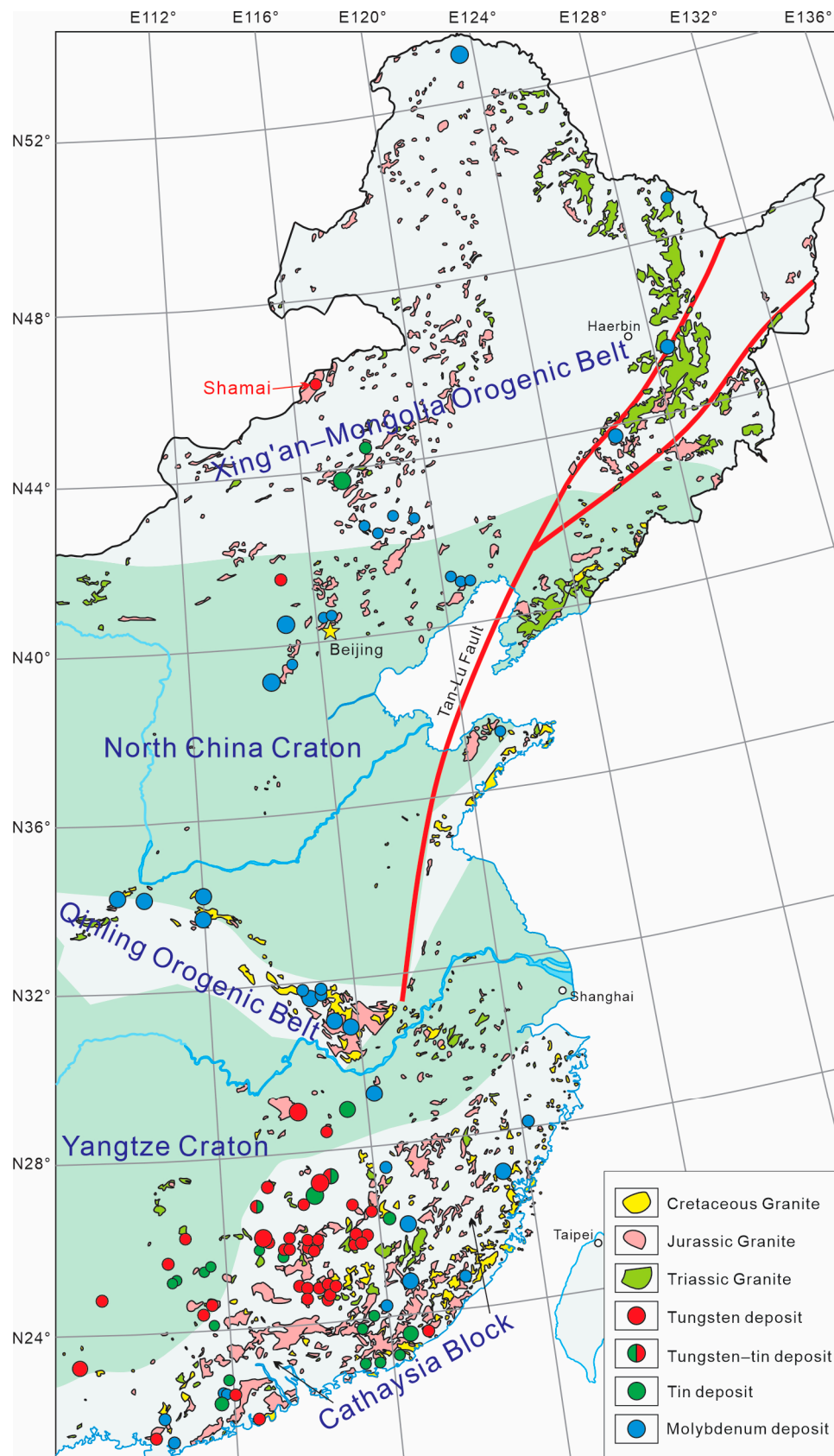
Figure 12. Distribution of Mesozoic tungsten, tin, and molybdenum deposits in East China. Tungsten, tin, and molybdenum deposit distribution was modified after [96]. The distribution of Mesozoic granite data is limited after [97]. The tectonic distribution of East China was modified after [98].

5.3. The Metallogenic Geodynamic Evolution of Tungsten in the XMOB

Many tungsten–tin deposits are linked to granites that originate from crustal-derived remelting. It is commonly believed that the development of quartz vein-type wolframite is closely associated with the remelting of the lower crust, which is driven by the upwelling of basaltic magma during lithospheric extension and collapse following orogeny. The ore-forming intrusions are mainly peraluminous crustal-derived granites [9,38]. To understand how tungsten deposits form in the XMOB, we summarized the Nd-Hf-Pb isotopic data from our analysis as well as data from previously published sources (Figures 13–15). The geochemical analysis yielded several key findings: Nd isotopes exhibit a clear linear evolutionary trend, with Nd(t) values rising as the age of mineralization decreases (see Figure 13). In contrast, Hf(t) isotopes in the Shamai tungsten deposit show a slight declining trend with age (see Figure 14b). Hf isotope analysis of ore-bearing intrusions in the tungsten ore districts of the Xing'an Block (Figure 14) shows that the magmatic source region is mainly derived from either a depleted mantle or a newly formed lower crust, with a notable inclination toward a newly formed lower crustal source εHf(t). In contrast, the tungsten origin in other areas within XMOB, particularly in deposits linked to copper and molybdenum, appears to be more complex, as indicated by the Nd(t) values (Figure 13) and Hf(t) isotopes (Figure 14). Furthermore, Pb isotopes suggest a crustal origin, mostly clustering within and near orogenic areas (Figure 15).
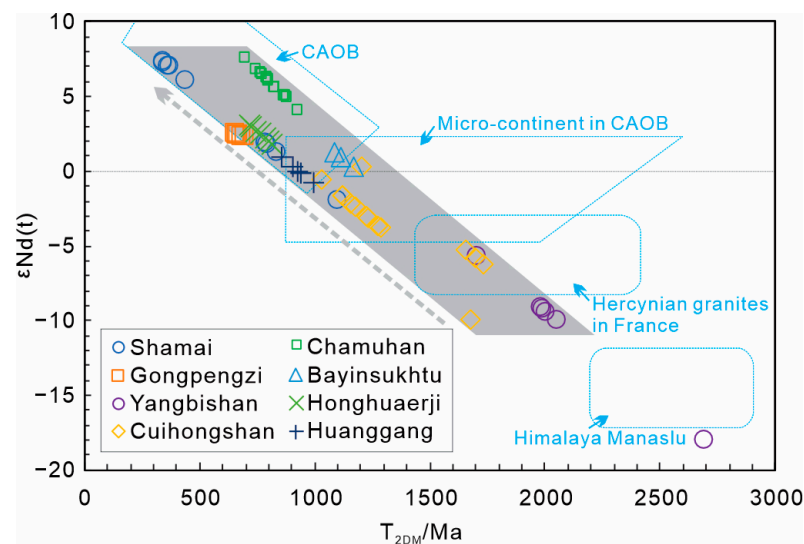
Figure 13. εNd(t) vs. T_{DM2} for igneous rocks from the tungsten deposits in northeast China. Data for the Shamai deposit are from [18,99]. Data for the Honghuaerji deposit are from [100]. Data for the Gongpengzi deposit are from [31]. Data for the Yangbishan deposit are from [25]. Data for the Cuihongshan deposit are from [28]. Data for the Bayinsukhtu deposit are from [65]. Data for the Huanggang deposit are from [33]. Data for the Chamuhan deposit are from [46]. The CAOB and microcontinent in the CAOB are from [101]. Hercynian granites in France are from [102,103]. Himalayan granites are from [104].
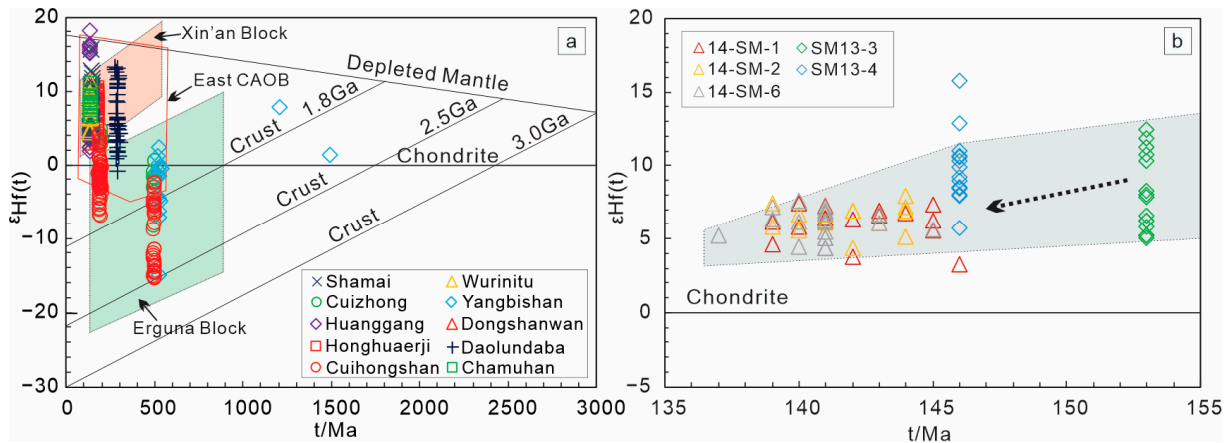
Figure 14. Correlations between εHf(t) and the U-Pb ages of zircon grains for the igneous rocks from the tungsten deposits in northeast China (**a**) and from the Shamai tungsten deposits (**b**). Data for the Shamai deposit are from this paper and [18]. Data for the Cuizhong deposit are from [105]. Data for the Dongshanwan deposit are from [47]. Data for the Wurinitu deposit are from [44]. Data for the Daolundaba deposit are from [41]. Data from the Huanggang deposit are from [33]. Data for the Yangbishan deposit are from [24]. Data for the Honghuaerji deposit are from [100]. Data for the Cuihongshan deposit are from [28]. Data for the Chamuhan deposit are from [46]. Groups of the East CAOB are from [106] and the Xing'an Block and Erguna Block from [42].
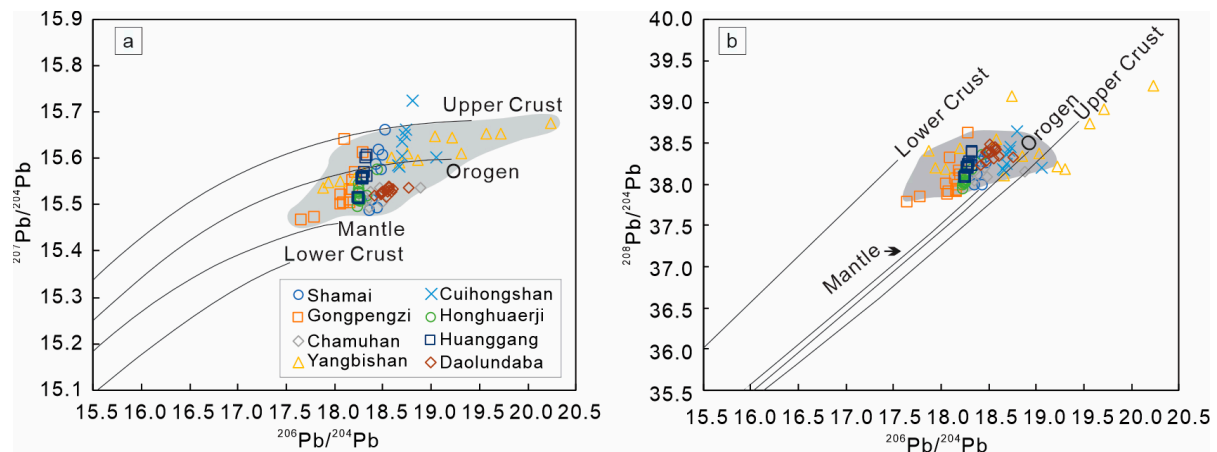
Figure 15. Evolution curve and tectonic environment discrimination diagrams of (**a**) ^{207}Pb/^{204}Pb vs. ^{206}Pb/^{204}Pb and (**b**) ^{208}Pb/^{204}Pb vs. ^{206}Pb/^{204}Pb (diagrams based on [107]) for samples from the tungsten deposits in northeast China. Data for the plagioclase of the Shamai deposit are from this paper. Data for the sulfides of the Gongpengzi deposit are from [31]. Data for the molybdenite of the Chamuhan deposit are from [46]. Data for the sulfides of the Yangbishan deposit are from [25,108]. Data for the sulfides of the Cuihongshan deposit are from [109]. Data for the sulfides and K-feldspar of the Honghuaerji deposit are from [12,100]. Data for the sulfides of the Huanggang deposit are from [34,110]. Data for biotite granite from the Daolundaba deposit are from [41].

Sun [111] elucidated the process of crustal evolution and its mechanisms in the Xing'an and Erguna regions. The primary factors driving crustal reworking include the breakup of the Precambrian supercontinent, the closure of the Paleo-Asian Ocean, and the evolution of the Mongol-Okhotsk and Paleo-Pacific tectonic regimes since the Phanerozoic. The mineralization of endogenetic ore deposits in the XMOB, which underwent intense magmatic activity during the Late Paleozoic and Mesozoic eras, is closely linked to the regional tectonic evolution [8,92,112]. Based on current research findings and considering variations in mineralization ages and tectonic settings, the tungsten mineralization periods in the XMOB

region can be divided into three stages: (1) Early Paleozoic (ca. 520–475 Ma); (2) Triassic (ca. 250–200 Ma); and (3) Jurassic to Early Cretaceous (ca. 190–130 Ma) (Figure 16).

In the Early Paleozoic (Figure 16a), only the Yangbishan tungsten deposit was identified in the Jiamusi Massif within the XMOB (Figure 1b, Table 1). Nd isotopes indicate that the ores originated from ancient crustal rocks [25], while Pb in the metal sulfides primarily derived from the ore-hosting strata and re-melted granitic magma [108] (Figure 15). This supports the notion that the interaction between crust-derived magma and strata rich in organics played a crucial role in the tungsten mineralization of the Yangbishan deposit [25,108]. Wu et al. [113] suggested that the Paleozoic granitoids formed during various stages, from oceanic subduction to block amalgamation in the CAOB. During the Early Ordovician, the Nenjiang Ocean between the Erguna–Xing'an united continent, and the Songnen Block began to subduct beneath the former [111], marking granitic magmatism between 530 and 515 Ma, followed by granulite/amphibolite facies metamorphism at approximately 500 Ma. Consequently, the Jiamusi Massif experienced both Pan-African and Late Paleozoic events [113]. The Paleozoic granitoids are not as extensively distributed in the area as previously believed [113], and the amalgamation of microblocks during this period [6] may have resulted in minimal tungsten mineralization in the XMOB (Figure 16a).
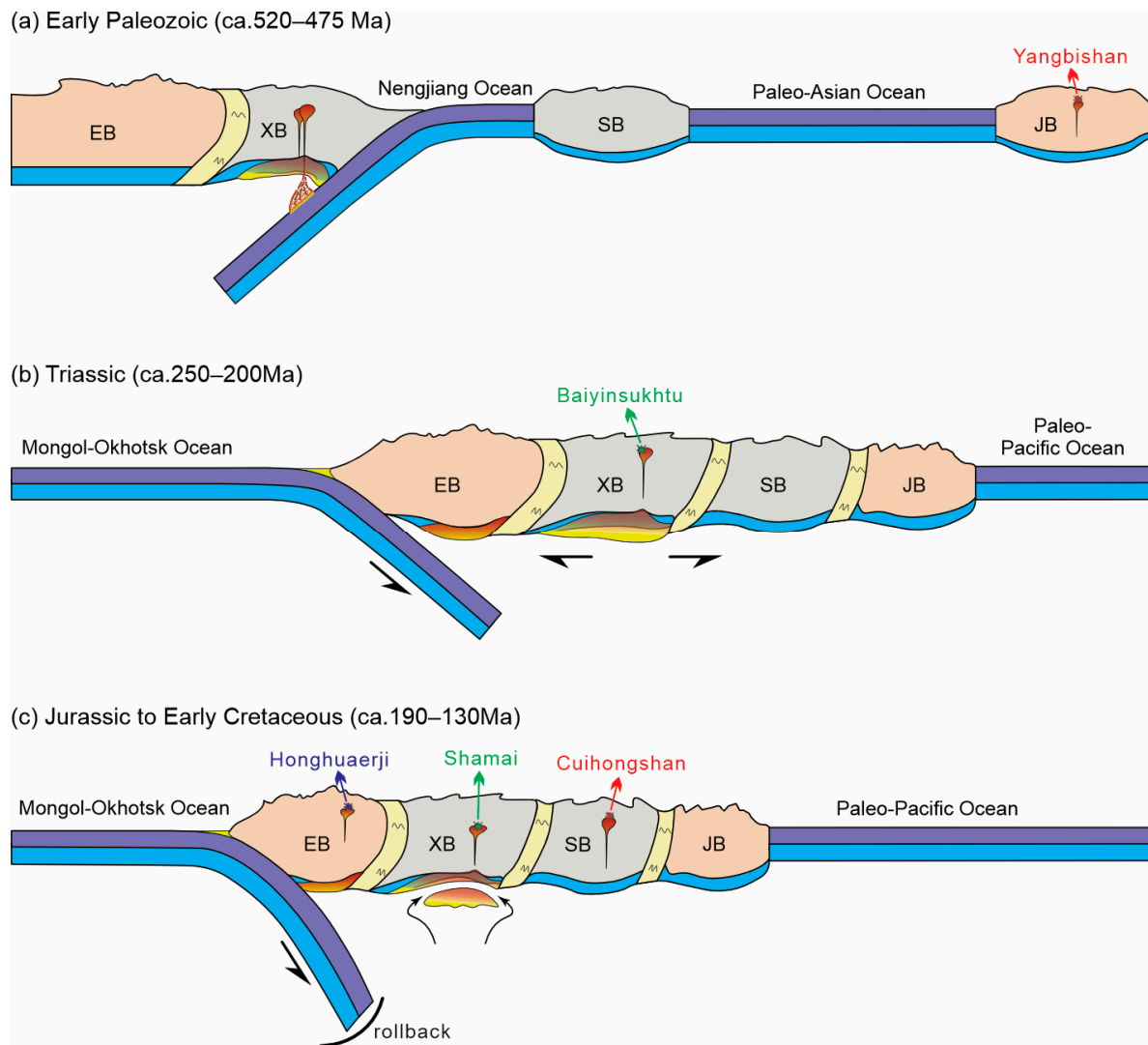
Figure 16. Tectonic evolution and tungsten mineralization model in the XMOB. The Early Paleozoic to Early Jurassic tectonic evolution in NE China is based on [114]. EB = Erguna Block; XB = Xing'an Block; SB = Songnen Block; JB = Jiamusi Block.

In the Triassic period (Figure 16b), tungsten deposits in the XMOB region were relatively small, consisting of only a few deposits like the Bayinsukhtu in the Xing'an Block and the Yangjingou and Wudaogou in the Xingkai Massif (Figure 1b; Table 1). The Nd isotopes, along with major and trace elements, suggest that the syenite porphyry in the Bayinsukhtu deposit formed during the transition from syn-collision to post-orogenic tectonic systems, characterized by an extensional geotectonic environment [65]. Crustal thickening and partial melting of crustal materials likely served as the primary dynamic mechanisms for granite formation in the Bayinsukhtu deposit [65]. The Yangjingou and Wudaogou vein-type tungsten deposits formed at an island–arc active continental margin in the Late Permian to Triassic period, when the subduction of the Paleo-Asian Ocean to the northeast block groups played an important role in the tectonic evolution of this area [23]. During the Early–Middle Triassic (Figure 16b), NE China was influenced by the Mongol-Okhotsk Ocean and the Paleo-Asian Ocean. The arc-type igneous rocks in the Erguna–Xing'an Block resulted from the southward subduction of the Mongol-Okhotsk Ocean Plate, while adakites with high Sr/Y and $(La/Yb)_N$ ratios in the southern segment of NE China were emplaced in a post-collision orogenic environment associated with the closure of the Paleo-Asian Ocean [115]. Based on the tectonic setting described above, compared to the formation mechanism of tungsten deposits in South China [9,95], the XMOB did not possess the conditions for large-scale tungsten mineralization during this period.

From the Jurassic to Early Cretaceous period (see Figure 16c), the highest tungsten mineralization concentration in the XMOB is located in the Xing'an Block (refer to Figure 1; Table 1). For instance, in the Shamai deposit, the zircon Hf(t) values for the fine- to medium-grained biotite monzogranite and porphyritic biotite monzogranite samples range from 3.2 to 7.9 and 4.2 to 7.6, respectively (see Supplementary Table S3). This yields T_{DM2} model ages of 996–692 Ma and 923–708 Ma, respectively. The initial $^{87}Sr/^{86}Sr$ ratios for these rock types are 0.70416 and 0.710350 [18]. Five wolframite samples from the deposit produced Nd(t) values ranging from 3.13 to 3.46 and Nd model ages (T_{DM2}) between 675 and 649 Ma, averaging 659 Ma. The Nd(t) values for the fine- to medium-grained and porphyritic biotite monzogranite intrusions span –1.86 to 7.44 and 1.28 to 6.95, respectively, corresponding to T_{DM2} ages of 1094–326 Ma and 867–327 Ma [18] (see Figure 13). The in situ Pb isotopic data for plagioclase from the Shamai tungsten deposit show similar trends (refer to Supplementary Table S4), plotting between the mantle and upper crustal evolution curves in Pb isotope evolution diagrams (see Figure 15). This suggests that the lead originates from either a deep mantle or upper crustal source. The geochemical resemblance between the fine- to medium-grained biotite monzogranite and porphyritic biotite monzogranite indicates that both types formed from primary magmas created by the partial melting of juvenile crustal material infused with mantle-derived components. Since the Mesozoic era, the XMOB has experienced extensional stress following the final closure of the Paleo-Asian Ocean, influenced by the tectonic evolution of the Mongol-Okhotsk Ocean and the Paleo-Pacific Ocean [112]. Two-stage subduction of the Paleo-Asian Ocean, coupled with a change in subduction direction, triggered two phases of arc igneous activity around 185–164 Ma and 135–120 Ma. The influence from the Mongol-Okhotsk Ocean domain ceased at approximately 120 Ma due to the rollback of the Paleo-Pacific oceanic slab [115]. This tectonic framework likely influences the Yanshanian magmatism and the prominent tungsten metallogenic events in the XMOB.

6. Conclusions

(1) The fine-grained biotite monzogranite, medium-grained biotite monzogranite, and porphyritic biotite monzogranite associated with the Shamai deposit yielded zircon U–Pb ages of 142.5 ± 1.0, 141.9 ± 1.1, and 140.2 ± 0.99 Ma, respectively. The geochemical,

zircon Hf isotopic, and in situ plagioclase Pb isotopic data for magmatic rocks from this deposit indicate that these granites formed from magmas generated by the partial melting of juvenile crustal material mixed with mantle-derived components.

(2) The tungsten mineralization periods in the XMOB region can be classified into three stages: Early Paleozoic (ca. 520–475 Ma), Triassic (ca. 250–200 Ma), and Jurassic to Early Cretaceous (ca. 190–130 Ma).

(3) The highest concentration of tungsten mineralization in the XMOB is found within the Xing'an Block during the Jurassic to Early Cretaceous period. An extensional setting and oceanic slab rollback, influenced by the Mongol-Okhotsk Ocean's and Paleo-Pacific Ocean's tectonic evolution, likely control the Yanshanian magmatism and the most significant tungsten metallogenic events.

References

1. Şengör, A.M.C.; Natal'In, B.A.; Sunal, G.; van der Voo, R. The tectonics of the altaids: Crustal growth during the construction of the continental lithosphere of central asia between ~750 and ~130 ma ago. *Annu. Rev. Earth Planet. Sci.* **2018**, *46*, 439–494. [CrossRef]
2. Windley, B.F.; Xiao, W.J. Ridge subduction and slab windows in the Central Asian Orogenic Belt: Tectonic implications for the evolution of an accretionary orogen. *Gondwana Res.* **2018**, *61*, 73–87. [CrossRef]
3. Xiao, W.; Song, D.; Windley, B.F.; Li, J.; Han, C.; Wan, B.; Zhang, J.; Ao, S.; Zhang, Z. Accretionary processes and metallogenesis of the Central Asian Orogenic Belt: Advances and perspectives. *Sci. China Earth Sci.* **2020**, *63*, 329–361. [CrossRef]

4. Ren, J.S.; Jiang, C.F.; Zhang, Z.K.; Qin, D.Y. *The Geotectonic Evolution of China*; Science Press: Beijing, China, 1980; pp. 1–50. (In Chinese)

5. Zhang, J.R.; Wei, C.J.; Chu, H. New model for the tectonic evolution of Xing' an-Inner Mongolia Orogenic Belt: Evidence from four different phases of metamorphism in Central Inner Mongolia. *Acta Petrol. Sin.* **2018**, *34*, 2857–2872. (In Chinese with English abstract).

6. Xu, W.; Sun, C.; Tang, J.; Luan, J.; Wang, F. Basement Nature and Tectonic Evolution of the Xing'an-Mongolian Orogenic Belt. *Diqiu Kexue—Zhongguo Dizhi Daxue Xuebao/Earth Sci.—J. China Univ. Geosci.* **2019**, *44*, 1620–1646. (In Chinese with English abstract).

7. Xu, B.; Wang, Z.W.; Zhang, L.Y.; Wang, Z.H.; Yang, Z.N.; He, Y. The Xing-Meng Intracontinent Orogenic Belt. *Acta Petrol. Sin.* **2018**, *34*, 2819–2844. (In Chinese with English abstract).

8. Jiang, S.; Zhang, L.; Liu, Y.; Liu, C.; Kang, H.; Wang, F. Metallogeny of Xing-Meng Orogenic Belt and some related problems. *Miner. Depos.* **2018**, *37*, 671–711. (In Chinese with English abstract).

9. Mao, J.; Ouyang, H.; Song, S.; Santosh, M.; Yuan, S.; Zhou, Z.; Zheng, W.; Liu, H.; Liu, P.; Cheng, Y.; et al. Geology and metallogeny of tungsten and tin deposits in China. *SEG Spec. Publ.* **2019**, *22*, 411–482.

10. Sheng, J.F.; Liu, L.J.; Wang, D.H.; Chen, Z.H.; Ying, L.J.; Huang, F.; Wang, J.H.; Zeng, L. A Preliminary Review of Metallogenic Regularity of Tungsten Deposits in China. *Acta Geol. Sin. (Engl. Ed.)* **2015**, *89*, 1359–1374. [CrossRef]

11. Xiang, A.P.; Wang, Y.J.; Qin, D.J.; She, H.Q.; Han, Z.G.; Guan, J.D.; Kang, Y.J. Metallogenic and diagenetic age of Honghuaerji tungsten polymetallic deposit in Inner Mongolia. *Miner. Depos.* **2014**, *33*, 428–439. (In Chinese with English abstract).

12. Guo, Z.J.; Li, J.W.; Xu, X.Y.; Song, Z.Y.; Dong, X.Z.; Tian, J.; Yang, Y.C.; She, H.Q.; Xiang, A.P.; Kang, Y.J. Sm-Nd dating and REE Composition of scheelite for the Honghuaerji scheelite deposit, Inner Mongolia, Northeast China. *Lithos* **2016**, *261*, 307–321. [CrossRef]

13. Hao, Y.J.; Ren, Y.S.; Zhao, H.L.; Zou, X.T.; Chen, C.; Hou, Z.S.; Qu, W. Re-Os Isotopic Dating of the Molybdenite from the Cuihongshan W-Mo Polymetallic Deposit in Heilongjiang Province and Its Geological Significance. *J. Jilin Univ. Earth Sci. Ed.* **2013**, *43*, 1840–1850. (In Chinese with English abstract).

14. Hu, X.-L.; Ding, Z.-J.; He, M.-C.; Yao, S.-Z.; Zhu, B.-P.; Shen, J.; Chen, B. Two epochs of magmatism and metallogeny in the Cuihongshan Fe-polymetallic deposit, Heilongjiang Province, NE China: Constrains from U–Pb and Re–Os geochronology and Lu–Hf isotopes. *J. Geochem. Explor.* **2014**, *143*, 116–126. [CrossRef]

15. Hu, P. Primary Geological and Geochemical Study of Shamai Tungsten Deposit in Inner Mongolia Autonomous Area. Master's Thesis, Northwest University, Xi'an, China, 2004; pp. 1–70. (In Chinese with English abstract).

16. Nie, F.J.; Hu, P.; Jiang, S.H.; Liu, Y.F. Geological Features, Geochronology and Origin of the Tungsten and Tungsten (Molybdenum) Deposits in the Shamai-Yuguzer Mineralization Concentrated Camp along the Sino-Mongolian Border. *Acta Geosci. Sin.* **2010**, *31*, 383–394. (In Chinese with English abstract).

17. Nie, F.J.; Jiang, S.H. Geological Setting and Origin of Mo–W–Cu Deposits in the Honggor–Shamai District, Inner Mongolia, North China. *Resour. Geol.* **2011**, *61*, 344–355. [CrossRef]

18. Jiang, S.-H.; Bagas, L.; Hu, P.; Han, N.; Chen, C.-L.; Liu, Y.; Kang, H. Zircon U–Pb ages and Sr–Nd–Hf isotopes of the highly fractionated granite with tetrad REE patterns in the Shamai tungsten deposit in eastern Inner Mongolia, China: Implications for the timing of mineralization and ore genesis. *Lithos* **2016**, *261*, 322–339. [CrossRef]

19. Mao, J.; Zheng, W.; Xie, G.; Lehmann, B.; Goldfarb, R. Recognition of a Middle–Late Jurassic arc-related porphyry copper belt along the southeast China coast: Geological characteristics and metallogenic implications. *Geology* **2021**, *49*, 592–596. [CrossRef]

20. Wu, Q.; Williams-Jones, A.E.; Zhao, P.; Yuan, S. The nature and origin of granitic magmas and their control on the formation of giant tungsten deposits. *Earth-Sci. Rev.* **2023**, *245*, 104554. [CrossRef]

21. Wu, F.-Y.; Zhao, G.-C.; Sun, D.-Y.; Wilde, S.A.; Yang, J.-H. The Hulan Group: Its role in the evolution of the Central Asian Orogenic Belt of NE China. *J. Asian Earth Sci.* **2007**, *30*, 542–556. [CrossRef]

22. Guo, Z.; Zhang, B.; Guo, B.; Dang, Y.; Hou, J. Zircon U-Pb and Wolframite Sm-Nd Dating of the Bayinsukhtu Tungsten Deposit in Southern Mongolia and its Geological Significance. *Resour. Geol.* **2018**, *68*, 337–351. [CrossRef]

23. Zhao, H.L. Ore Genesis and Geodynamic Settings of Tungsten Deposits in Eastern Jilin and Heilongjiang Provinces. Ph.D. Thesis, Jilin University, Changchun, China, 2014; pp. 1–150. (In Chinese with English abstract).

24. Hao, Y.; Ren, Y.; Zhao, H.; Lai, K.; Zhao, X.; Ma, Y. Metallogenic mechanism and tectonic setting of tungsten mineralization in the yangbishan deposit in Northeastern China. *Acta Geol. Sin. Engl. Ed.* **2018**, *92*, 241–267. [CrossRef]

25. Hao, Y.; Ren, Y.; Yang, Q.; Sun, Z.; Ma, Y.; Lai, K. Fluid and ore sources of the tungsten mineralisation in the Yangbishan iron-tungsten deposit, Heilongjiang Province, North-eastern China: Constraints from fluid inclusions, sulphide S-Pb isotopes and scheelite C-H-O-Sm-Nd isotopes. *Geol. J.* **2020**, *55*, 3957–3976. [CrossRef]

26. Zhao, H.L.; Ren, Y.S.; Ju, N.; Wang, H.; Hou, K.J. Geochronology and Geochemistry of Metallogenic Intrusion in Baishilazi Tungsten Deposit of Eastern Yanbian Area, Northeast China. *J. Jilin Univ. Earth Sci. Ed.* **2011**, *41*, 1726–1735,1744. (In Chinese with English abstract).

27. Chen, X.; Liu, J.; Carranza, E.J.M.; Zhang, D.; Collins, A.; Yang, B.; Xu, B.; Zhai, D.; Wang, Y.; Wang, J.; et al. Geology, geochemistry, and geochronology of the Cuihongshan Fe-polymetallic deposit, Heilongjiang Province, NE China. *Geol. J.* **2018**, *54*, 1254–1278. [CrossRef]

28. Fei, X.; Zhang, Z.; Cheng, Z.; Santosh, M.; Jin, Z.; Wen, B.; Li, Z.; Xu, L. Highly differentiated magmas linked with polymetallic mineralization: A case study from the Cuihongshan granitic intrusions, Lesser Xing'an Range, NE China. *Lithos* **2018**, *302*, 158–177. [CrossRef]

29. Ren, Y.S.; Niu, J.P.; Wang, H.; Lei, E. LA-ICP-MS Zircon U-Pb age and its geological significance of tungsten-bearing Mengjialing ganitic intrusion in Siping area, Jilin Province. *J. Mineral. Petrol.* **2009**, *29*, 100–105. (In Chinese with English abstract).

30. Ren, Y.S.; Niu, J.P.; Lei, E.; Wang, H.; Wang, X. Geological & Geochemical Characteristics and Metallogenesis of Sanjiazi Scheelite Deposit in Siping Area, Jilin Province. *J. Jilin Univ. Earth Sci. Ed.* **2010**, *40*, 314–320. (In Chinese with English abstract).

31. Li, Y.; Yu, X.; Mi, K.; Carranza, E.J.M.; Liu, J.; Jia, W.; He, S. Deposit geology, geochronology and geochemistry of the Gongpengzi skarn Cu-Zn-W polymetallic deposit, NE China. *Ore Geol. Rev.* **2019**, *109*, 465–481. [CrossRef]

32. Zhou, Z.H.; Lue, L.S.; Feng, J.R.; Li, C.; Li, T. Molybdenite Re-Os ages of Huanggang skarn Sn-Fe deposit and their geological significance, Inner Mongolia. *Acta Petrol. Sin.* **2010**, *26*, 667–679. (In Chinese with English abstract).

33. Zhou, Z.-H.; Mao, J.-W.; Lyckberg, P. Geochronology and isotopic geochemistry of the A-type granites from the Huanggang Sn–Fe deposit, southern Great Hinggan Range, NE China: Implication for their origin and tectonic setting. *J. Asian Earth Sci.* **2012**, *49*, 272–286. [CrossRef]

34. Mei, W.; Lu, X.B.; Cao, X.F.; Liu, Z.; Zhao, Y.; Ai, Z.L.; Tang, R.K.; Abfaua, M.M. Ore genesis and hydrothermal evolution of the Huanggang skarn iron–tin polymetallic deposit, southern Great Xing'an Range: Evidence from fluid inclusions and isotope analyses. *Ore Geol. Rev.* **2015**, *64*, 239–252. [CrossRef]

35. Wang, Y.; Wang, K.; Konare, Y. N2-rich fluid in the vein-type Yangjingou scheelite deposit, Yanbian, NE China. *Sci. Rep.* **2018**, *8*, 5662. [CrossRef]

36. Liu, Y.; Nie, F.J.; Liu, Y.F.; Hou, W.R. Zircon SHRIMP U-Pb dating and geological significance of granite in the Baogeda Ula Mo (W) mining area, Inner Mongolia, China. *Acta Petrol. Sin.* **2012**, *28*, 401–408. (In Chinese with English abstract).

37. Chen, C.; Ren, Y.S.; Zhao, H.L.; Yang, Q.; Zou, X.T.; Hou, K.J.; Jiang, G.H. Geochronology, geochemistry and metallogenic significance of Wudaogou granodiorite intrusion in eastern Yanbian, NE China. *J. Cent. South Univ. (Sci. Technol.)* **2015**, *46*, 2962–2974. (In Chinese with English abstract).

38. Xiang, A.P. Tungsten and Molybdenum mineralization mechanism of Dongwuqi to Nenjiang Metallogenic belt and its geodynamic setting, Inner Mongolia. Ph.D. Thesis, China University of Geosciences, Wuhan, China, 2016; pp. 1–206. (In Chinese with English abstract).

39. Xiang, A.; Chen, Y.; She, H.; Li, G.; Li, Y. Chronology and geochemical characteristics of granite in Weilianhe of Inner Mongolia and its geological significance. *Geol. China* **2018**, *45*, 963–976. (In Chinese with English abstract).

40. Xiang, A.P.; Chen, Y.C.; Bagas, L.; She, H.Q.; Kang, Y.J.; Yang, W.S.; Li, C.J. Molybdenite Re–Os and U–Pb zircon dating and genesis of the Dayana W-Mo deposit in eastern Ujumchin, Inner Mongolia. *Ore Geol. Rev.* **2016**, *78*, 268–280. [CrossRef]

41. Zhou, Z.H.; Ouyang, H.G.; Wu, X.L.; Liu, J.; Che, H.W. Geochronology and geochemistry study of the biotite granite from the Daolundaba Cu-W polymetallic deposit in the Inner Mongolia and its geological significance. *Acta Petrol. Sin.* **2014**, *30*, 79–94. (In Chinese with English abstract).

42. Feng, Z.; Liu, Y.; Li, Y.; Li, W.; Wen, Q.; Liu, B.; Zhou, J.; Zhao, Y. Ages, geochemistry and tectonic implications of the Cambrian igneous rocks in the northern Great Xing'an Range, NE China. *J. Asian Earth Sci.* **2017**, *144*, 5–21. [CrossRef]

43. Liu, C.; Deng, J.; Kong, W.; Xu, L.; Zhao, G.; Luo, Z.; Li, N. LA-ICP-MS Zircon U-Pb Geochronology of the Fine-grained Granite and Molybdenite Re-Os Dating in the Wurinitu Molybdenum Deposit, Inner Mongolia, China. *Acta Geol. Sin. Engl. Ed.* **2011**, *85*, 1057–1066. [CrossRef]

44. Zhang, Z.J.; Cheng, Q.M.; Yao, L.Q.; Bai, H.S.; Li, C. Zircon U-Pb-Hf Isotopic Systematics and Geochemistry of the Granites in the Wurinitu Molybdenum Deposit, Inner Mongolia, China: Implications for Tectonic Setting and Genetic Type of Mineralization. *Acta Geol. Sin. Engl. Ed.* **2016**, *90*, 2066–2079. [CrossRef]

45. Liu, Y.F.; Jiang, S.H.; Bagas, L. The genesis of metal zonation in the Weilasituo and Bairendaba Ag-Zn-Pb-Cu-(Sn-W) deposits in the shallow part of a porphyry Sn-W-Rb system, Inner Mongolia, China. *Ore Geol. Rev.* **2016**, *75*, 150–173. [CrossRef]

46. Zhang, L.; Jiang, S.; Bagas, L.; Han, N.; Liu, Y.; Liu, Y. Element behaviour during interaction of magma and fluid: A case study of Chamuhan Granite, and implications on the genesis of W–Mo mineralisation. *Lithos* **2019**, *342–343*, 31–44. [CrossRef]

47. Zeng, Q.-D.; Sun, Y.; Chu, S.-X.; Duan, X.-X.; Liu, J.M. Geochemistry and geochronology of the Dongshanwan porphyry Mo–W deposit, Northeast China: Implications for the Late Jurassic tectonic setting. *J. Asian Earth Sci.* **2015**, *97*, 472–485. [CrossRef]

48. Xiao, W.J.; Windley, B.F.; Hao, J.; Zhai, M.G. Accretion leading to collision and the Permian Solonker suture, Inner Mongolia, China: Termination of the central Asian orogenic belt. *Tectonics* **2003**, *22*, 1069. [CrossRef]

49. Kovalenko, V.I.; Yarmoluyk, V.V.; Sal'nikova, E.B.; Kozlovsky, A.M.; Kotov, A.B.; Kovach, V.P.; Savatenkov, V.M.; Vladykin, N.V.; Ponomarchuk, V.A. Geology, Geochronology, and Geodynamics of the Khan Bogd alkali granite pluton in southern Mongolia. *Geotectonics* **2006**, *40*, 450–466. [CrossRef]

50. Li, J.-Y. Permian geodynamic setting of Northeast China and adjacent regions: Closure of the Paleo-Asian Ocean and subduction of the Paleo-Pacific Plate. *J. Asian Earth Sci.* **2006**, *26*, 207–224. [CrossRef]

51. Windley, B.F.; Maruyama, S.; Xiao, W.J. Delamination/thinning of sub-continental lithospheric mantle under Eastern China: The role of water and multiple subduction. *Am. J. Sci.* **2010**, *310*, 1250–1293. [CrossRef]

52. Xu, B.; Charvet, J.; Chen, Y.; Zhao, P.; Shi, G.Z. Middle Paleozoic convergent orogenic belts in western Inner Mongolia (China): Framework, kinematics, geochronology and implications for tectonic evolution of the Central Asian Orogenic Belt. *Gondwana Res.* **2013**, *23*, 1342–1364. [CrossRef]

53. Ruppen, D.; Knaf, A.; Bussien, D.; Winkler, W.; Chimedtseren, A.; von Quadt, A. Restoring the Silurian to Carboniferous northern active continental margin of the Mongol–Okhotsk Ocean in Mongolia: Hangay–Hentey accretionary wedge and seamount collision. *Gondwana Res.* **2014**, *25*, 1517–1534. [CrossRef]

54. Liu, B.; Han, B.-F.; Xu, Z.; Ren, R.; Zhang, J.-R.; Zhou, J.; Su, L.; Li, Q.-L. The Cambrian initiation of intra-oceanic subduction in the southern Paleo-Asian Ocean: Further evidence from the Barleik subduction-related metamorphic complex in the West Junggar region, NW China. *J. Asian Earth Sci.* **2016**, *123*, 1–21. [CrossRef]

55. Xu, B.; Zhao, P.; Wang, Y.Y.; Liao, W.; Luo, Z.W.; Bao, Q.Z.; Zhou, Y.H. The pre-Devonian tectonic framework of Xing'an–Mongolia orogenic belt (XMOB) in north China. *J. Asian Earth Sci.* **2015**, *97*, 183–196. [CrossRef]

56. Jian, P.; Kröner, A.; Windley, B.F.; Shi, Y.; Zhang, W.; Zhang, L.; Yang, W. Carboniferous and Cretaceous mafic–ultramafic massifs in Inner Mongolia (China): A SHRIMP zircon and geochemical study of the previously presumed integral "Hegenshan ophiolite". *Lithos* **2012**, *142–143*, 48–66. [CrossRef]

57. Zhang, W.Y. Magmatic Activity and Metallogeny of Dong Ujimqin Banner, Inner Mongolia. Ph.D. Thesis, Chinese Academy of Geological Sciences, Beijing, China, 2008; pp. 1–179. (In Chinese with English abstract).

58. Liu, Y.S.; Hu, Z.C.; Zong, K.Q.; Gao, C.G.; Gao, S.; Xu, J.; Chen, H.H. Reappraisement and refinement of zircon U-Pb isotope and trace element analyses by LA-ICP-MS. *Chin. Sci. Bull.* **2010**, *55*, 1535–1546. [CrossRef]

59. Andersen, T. Correction of common lead in U–Pb analyses that do not report 204Pb. *Chem. Geol.* **2002**, *192*, 59–79. [CrossRef]

60. Ludwig, K.R. User's manual for Isoplot 3.00: A geochronological toolkit for Microsoft Excel. *Berkeley Geochronl. Cent. Spec. Publ.* **2003**, *4*, 25–32.

61. Xu, P.; Wu, F.Y.; Xie, L.W.; Yang, Y.H. Hf isotopic compositions of the standard zircons for U-Pb dating. *Chin. Sci. Bull.* **2004**, *49*, 1642–1648. [CrossRef]

62. Wu, F.-Y.; Yang, Y.-H.; Xie, L.-W.; Yang, J.-H.; Xu, P. Hf isotopic compositions of the standard zircons and baddeleyites used in U–Pb geochronology. *Chem. Geol.* **2006**, *234*, 105–126. [CrossRef]

63. Zhang, L.; Ren, Z.-Y.; Nichols, A.R.; Zhang, Y.-H.; Zhang, Y.; Qian, S.-P.; Liu, J.-Q. Lead isotope analysis of melt inclusions by LA-MC-ICP-MS. *J. Anal. At. Spectrom.* **2014**, *29*, 1393–1405. [CrossRef]

64. Sun, S.S.; McDonough, W.F. Chemical and isotopic systematics of oceanic basalts: Implications for mantle composition and processes. In *Magmatism in the Ocean Basin*; Geological Society Special Publication: London, UK, 1989; Volume 42, pp. 313–345.

65. Guo, Z.; Zhang, B.; Dang, Y.; Guo, B.; Gao, L.; Hou, J.; Zhang, L. Zircon U-Pb Ages and Its Significance of the Syenite Porphyry in Bayinsuhetu Tungsten Deposit, Mongolia. *Geol. Rev.* **2017**, *63*, 1378–1390. (In Chinese with English abstract).

66. Dong, Y.; Wang, S.; Yu, Q.; Chen, J.; Yang, H.; Ge, W.; Bi, J.; Jing, J. Late Paleozoic tectonic -magmatic evolution history of the northeastern China. *Acta Petrol. Sin.* **2022**, *38*, 2249–2268. (In Chinese with English abstract).

67. Li, J.J.; Fu, C.; Tang, W.L.; Li, H.M.; Lin, Y.X.; Zhang, T.; Wang, S.G.; Zhao, Z.L.; Dang, Z.C.; Zhao, L.J. Shamai wolframite deposit in Dong Ujimqin Banner, Inner Mongolia. *Geol. Bull. China* **2016**, *35*, 524–530. (In Chinese with English abstact).

68. Taylor, R.G. *Geology of Tin Deposits*; Elsevier: Amsterdam, The Netherlands, 1979; pp. 1–543.

69. Štemprok, M. A comparison of the Krušné hory-Erzgebirge (Czech Republic-Germany) and Cornish (UK) granites and their related mineralisation. *Geosci. South-West Engl.* **1995**, *8*, 347–356.

70. Romer, R.L.; Kroner, U. Phanerozoic tin and tungsten mineralization—Tectonic controls on the distribution of enriched protoliths and heat sources for crustal melting. *Gondwana Res.* **2016**, *31*, 60–95. [CrossRef]

71. Yang, W.S. The Study of the Magma Effect in the Region of Dong Ujimqin Banner, Inner Mongolia, and the Metallogenic Relationship of Tungsten Molybdenum and Polymetallic Deposits. Master's Thesis, Chinese Academy of Geological Sciences, Beijing, China, 2017; pp. 1–69. (In Chinese with English abstract).

72. Shu, X.-J.; Wang, X.-L.; Sun, T.; Xu, X.; Dai, M.-N. Trace elements, U–Pb ages and Hf isotopes of zircons from Mesozoic granites in the western Nanling Range, South China: Implications for petrogenesis and W–Sn mineralization. *Lithos* **2011**, *127*, 468–482. [CrossRef]

73. Huang, L.-C.; Jiang, S.-Y. Highly fractionated S-type granites from the giant Dahutang tungsten deposit in Jiangnan Orogen, Southeast China: Geochronology, petrogenesis and their relationship with W-mineralization. *Lithos* **2014**, *202–203*, 207–226. [CrossRef]

74. Mao, Z.-H.; Liu, J.-J.; Mao, J.-W.; Deng, J.; Zhang, F.; Meng, X.-Y.; Xiong, B.-K.; Xiang, X.-K.; Luo, X.-H. Geochronology and geochemistry of granitoids related to the giant Dahutang tungsten deposit, middle Yangtze River region, China: Implications for petrogenesis, geodynamic setting, and mineralization. *Gondwana Res.* **2015**, *28*, 816–836. [CrossRef]

75. Peccerillo, A.; Taylor, S.R. Geochemistry of eocene calc-alkaline volcanic rocks from the Kastamonu area, Northern Turkey. *Contrib. Miner. Petrol.* **1976**, *58*, 63–81. [CrossRef]

76. Maniar, P.D.; Piccoli, P.M. Tectonic discrimination of granitoids. *Geol. Soc. Am. Bull.* **1989**, *101*, 635–643. [CrossRef]

77. Chappell, B.W. Aluminium saturation in I- and S-type granites and the characterization of fractionated haplogranites. *Lithos* **1999**, *46*, 535–551. [CrossRef]

78. Chappell, B.W.; White, A.J.R. I- and S-type granites in the Lachlan Fold Belt. *Earth Environ. Sci. Trans. R. Soc. Edinb.* **1992**, *83*, 1–26. [CrossRef]

79. Thorn, P.G. Fluid inclusion and stable isotope studies at the Chicote tungsten deposit, Bolivia. *Econ. Geol.* **1988**, *83*, 62–68. [CrossRef]

80. Gibert, F.; Moine, B.; Schott, J.; Dandurand, J.-L. Modeling of the transport and deposition of tungsten in the scheelite-bearing calc-silicate gneisses of the Montagne Noire, France. *Contrib. Miner. Pet.* **1992**, *112*, 371–384. [CrossRef]

81. Xi, B.B.; Zhang, D.H.; Zhou, L.M.; Zhang, W.H.; Wang, C. Characteristics of Ore-forming Fluid Evolution in Dajishan Tungsten Deposit, Quannan County, Jiangxi. *Acta Geol. Sin.* **2008**, *82*, 956–966. (In Chinese with English abstract).

82. Polya, D.A. Chemistry of the main-stage ore-forming fluids of the Panasqueira W-Cu(Ag)-Sn deposit, Portugal; implications for models of ore genesis. *Econ. Geol.* **1989**, *84*, 1134–1152. [CrossRef]

83. O'Reilly, C.; Gallagher, V.; Feely, M. Fluid inclusion study of the Ballinglen W-Sn-sulphide mineralization, SE Ireland. *Miner. Depos.* **1997**, *32*, 569–580. [CrossRef]

84. Gong, Q.J.; Yu, C.W.; Zhang, R.H. Physical chemistry study on the ore-forming process of Shizhuyuan tungsten-polymetallic deposit. *Earth Sci. Front.* **2004**, *11*, 617–625. (In Chinese with English abstract).

85. Higgins, N.C. Fluid inclusion evidence for the transport of tungsten by carbonate complexes in hydrothermal solutions. *Can. J. Earth Sci.* **1980**, *17*, 823–830. [CrossRef]

86. Higgins, N.C. Wolframite deposition in a hydrothermal vein system; the Grey River tungsten prospect, Newfoundland, Canada. *Econ. Geol.* **1985**, *80*, 1297–1327. [CrossRef]

87. Graupner, T.; Kempe, U.; Dombon, E.; Pätzold, O.; Leeder, O.; Spooner, E.T.C. Fluid regime and ore formation in the tungsten(–yttrium) deposits of Kyzyltau (Mongolian Altai): Evidence for fluid variability in tungsten–tin ore systems. *Chem. Geol.* **1999**, *154*, 21–58. [CrossRef]

88. Kelly, W.C.; Rye, R.O. Geologic, fluid inclusion, and stable isotope studies of the tin-tungsten deposits of Panasqueira, Portugal. *Econ. Geol.* **1979**, *74*, 1721–1822. [CrossRef]

89. Wei, W.; Hu, R.; Bi, X.; Peng, J.; Su, W.; Song, S.; Shi, S. Infrared microthermometric and stable isotopic study of fluid inclusions in wolframite at the Xihuashan tungsten deposit, Jiangxi province, China. *Miner. Depos.* **2012**, *47*, 589–605. [CrossRef]

90. Hu, P.; Nie, F.J.; He, Y.; Zhang, Y.; Liu, Y. Geological features and fluid inclusions of Shamai tungsten deposit, Inner Mongolia. *Miner. Depos.* **2005**, *24*, 603–612. (In Chinese with English abstract).

91. Li, H.B.; Xie, Y.L. Study on fluid inclusion of the pegmatite in Shamai deposit, Inner Mongolia. *Acta Mineral. Sin.* **2015**, *35*, 592. (In Chinese)

92. Lü, B.; Wang, T.; Tong, Y.; Zhang, L.; Yang, Q.D.; Zhang, J.J. Spatial & Temporal Distribution and Tectonic Settings of Magmatic-Hydrothermal Ore Deposits in the Eastern Central Asia Orogen Belt. *J. Jilin Univ. (Earth Sci. Ed.)* **2017**, *47*, 305–343. (In Chinese with English abstract).

93. Mao, J.W.; Xie, G.Q.; Guo, C.L.; Yuan, S.D.; Chen, Y.B.; Chen, Y.C. Spatial-Temporal Distribution of Mesozoic Ore Deposits in South China and Their Metallogenic Settings. *Geol. J. China Univ.* **2008**, *14*, 510–526. (In Chinese with English abstract).

94. Hua, R.M.; Li, G.L.; Zhang, W.L.; Hu, D.Q.; Chen, P.R.; Chen, W.F.; Wang, X.D. A tentative discussion on differences between large-scale tungsten and tin mineralizations in South China. *Miner. Depos.* **2010**, *29*, 9–23. (In Chinese with English abstract).

95. Zhu, H.L.; Zhang, L.P.; Du, L.; Sui, Q.L. The geochemical behavior of tungsten and the genesis of tungsten deposits in South China. *Acta Petrol. Sin.* **2020**, *36*, 13–22. (In Chinese with English abstract).

96. Mao, J.; Pirajno, F.; Cook, N. Mesozoic metallogeny in East China and corresponding geodynamic settings—An introduction to the special issue. *Ore Geol. Rev.* **2011**, *43*, 1–7. [CrossRef]

97. Qiao, H.; Zhen, Y.Q. Sub-mantle plume structure-the main Mesozoic-Cenozoic mineral resources-control factor in East China. *Contrib. Geol. Miner. Resour. Res.* **2014**, *29*, 31–43. (In Chinese with English abstract).

98. Pan, G.T.; Xiao, Q.H.; Lu, S.N.; Den, J.F.; Feng, Y.M.; Zhang, K.X.; Zhang, Z.Y.; Wang, F.G.; Xing, G.F.; Hao, G.J.; et al. Subdivision of tectonic units in China. *Geol. Chin* **2009**, *36*, 1–28. (In Chinese with English abstract).

99. Hu, P.; Nie, F.; He, Y.; Zhang, Y.; Liu, Y. A peraluminous granite with positive εNd(t) values: The Shamai pluton in Inner Mongolia, northeast China. *Acta Petrol. Sin.* **2006**, *22*, 2781–2790. (In Chinese with English abstract).

100. Guo, Z.J.; Li, J.W.; Huang, G.J.; Guan, J.D.; Dong, X.Z.; Tian, J.; Yang, Y.C.; She, H.-Q.; Xiang, A.P.; Kang, Y.J. Sr-Nd-Pb-Hf isotopic characteristics of ore-bearing granites in the Honghuaerji scheelite deposit, Inner Mongolia. *Geol. China* **2014**, *41*, 1226–1241. (In Chinese with English abstract).

101. Hong, D.W.; Wang, S.G.; Xie, X.L.; Zhang, J.S. Genesis of positive ε (Nd, t) granitoids in the Da Hinggan Mts.–Mongolia orogenic belt and growth continental crust. *Earth Sci. Front.* **2000**, *7*, 441–456. (In Chinese with English abstract).

102. Bernard-Griffiths, J.; Peucat, J.J.; Sheppard, S.; Vidal, P. Petrogenesis of Hercynian leucogranites from the southern Armorican Massif: Contribution of REE and isotopic (Sr, Nd, Pb and O) geochemical data to the study of source rock characteristics and ages. *Earth Planet. Sci. Lett.* **1985**, *74*, 235–250. [CrossRef]

103. Downes, H.; Shaw, A.; Williamson, B.; Thirlwall, M.F. Sr, Nd and Pb isotope geochemistry of the Hercynian granodiorites and monzogranites, Massif Central, France. *Chem. Geol.* **1997**, *136*, 99–122. [CrossRef]

104. Vidal, P.; Bernard-Griffiths, J.; Cocherie, A.; Le Fort, P.; Peucat, J.J.; Sheppard, S.M.F. Geochemical comparison between Himalayan and Hercynian leucogranites. *Phys. Earth Planet. Inter.* **1984**, *35*, 179–190. [CrossRef]

105. Yang, J.; Hu, X.; Li, C.; Dong, Z.; Zeng, G.; Yao, S. Petrogenic and Metallogenic Geochronology, Geochemical Characteristics and Its Geological Implications of Cuizhong Fe Polymetallic Deposit, Heilongjiang Province. *Earth Sci.* **2020**, *45*, 1593–1608. (In Chinese with English abstract).

106. Yang, J.-H.; Wu, F.-Y.; Shao, J.-A.; Wilde, S.A.; Xie, L.-W.; Liu, X.-M. Constraints on the timing of uplift of the Yanshan Fold and Thrust Belt, North China. *Earth Planet. Sci. Lett.* **2006**, *246*, 336–352. [CrossRef]

107. Zartman, R.E.; Doe, B.R. Plumbotectonics—The model. *Tectonophysics* **1981**, *75*, 135–162. [CrossRef]

108. Ma, Y.P.; Ren, Y.S.; Hao, Y.J.; Lai, K.; Zhao, H.L.; Liu, J. Ore genesis and material source of scheelite mineralization of Yangbishan iron-tungsten deposit in Heilongjiang Province, NE China. *J. Jilin Univ. Earth Sci. Ed.* **2018**, *48*, 105–117. (In Chinese with English abstract).

109. Chen, X.; Liu, J.J.; Zhang, D.H.; Zhang, Q.B.; Yang, S.S.; Li, Y.C.; Cao, Q. Re-Os dating of molybdenites and S-Pb isotopic characteristics of the Cuihongshan iron polymetallic deposit, Heilongjiang Province. *Acta Petrol. Sin.* **2017**, *33*, 529–544. (In Chinese with English abstract).

110. Yao, M.J.; Liu, J.J.; Zhai, D.G.; Wang, J.P.; Xing, Y.L. Sulfur and lead isotopic compositions of the polymetallic deposits in the southern Daxing'anling: Implications for metal sources. *J. Jilin Univ. (Earth Sci. Ed.)* **2012**, *42*, 362–373. (In Chinese with English abstract).

111. Sun, C.Y. Crustal Growth and Reworking Processes of the Erguna and Xing'an Massifs: Evidence from Granitoids. Ph.D. Thesis, Jilin University, Changchun, China, 2022; pp. 1–172. (In Chinese with English abstract).

112. Xu, C.H. Metallogenesis of Endogenetic Metal Deposits in the Great Xing'an Range, NE China. Ph.D. Thesis, Jilin University, Changchun, China, 2023; pp. 1–273. (In Chinese with English abstract).

113. Wu, F.Y.; Sun, D.Y.; Ge, W.C.; Zhang, Y.B.; Grant, M.L.; Wilde, S.A.; Jahn, B.M. Geochronology of the Phanerozoic granitoids in northeastern China. *J. Asian Earth Sci.* **2011**, *41*, 1–30. [CrossRef]

114. Zhao, C.; Qin, K.-Z.; Song, G.-X.; Li, G.-M. Switch of geodynamic setting from the Paleo-Asian Ocean to the Mongol-Okhotsk Ocean: Evidence from granitoids in the Duobaoshan ore field, Heilongjiang Province, Northeast China. *Lithos* **2019**, *336–337*, 202–220. [CrossRef]

115. Wu, Z.; Yang, X.; Ma, Y.; Sun, S.; Han, X.; Zheng, Y.; Li, S. A synthesis of geochemistry of Mesozoic igneous rocks in NE China and tectonic superposition and transformation of the easternmost Central Asian Orogenic Belt. *J. Asian Earth Sci.* **2022**, *227*, 105032. [CrossRef]